Establishing genetic relationships between the Takidani pluton and two large silicic eruptions in the Northern Japan Alps

Hartung, Eva; Caricchi, Luca; Floess, David; Wallis, Simon; Harayama, Satoru

Establishing genetic relationships between the Takidani pluton and two large silicic eruptions in the Northern Japan Alps

Eva Hartung[1,2], Luca Caricchi[2], David Floess[2], Simon Wallis[3], Satoru Harayama[4]

[1]*Department of Earth, Ocean and Ecological Sciences, University of Liverpool, Liverpool L69 3GP, United Kingdom*

[2]*Department of Earth Sciences, University of Geneva, Geneva 1205, Switzerland*

[3]*Department of Earth and Planetary Science, The University of Tokyo, Tokyo 113-0033, Japan*

[4]*Department of Geology, Shinshu University, Matsumoto 390-8621, Japan*

ABSTRACT

The Takidani pluton (1.1-1.6 Ma) represents a shallow magmatic reservoir at the base of an exhumed caldera floor. The deposits of two large caldera-forming eruptions including the Nyukawa Pyroclastic Flow Deposit (1.76 Ma; crystal-rich dacite) and the Chayano Tuff and Ebisutoge Pyroclastic Deposits (1.75 Ma; a sequence of crystal-poor rhyolite) are distributed concentrically around the pluton. We use major and trace element chemistry of whole-rock, glass and minerals to show (1) that the crystal-rich dacite (>400 km^3 DRE; dense rock equivalent) is the erupted portion of a shallow mush zone constituting the Takidani pluton and (2) that the crystal-poor rhyolite (>100 km^3 DRE) was extracted from a deeper part of this vertically extended magmatic plumbing system. Whole-rock geochemistry indicates that the Nyukawa and Takidani compositions were produced dominantly through crystal fractionation of amphibole, pyroxene and plagioclase in the mid-to-lower crust and subsequently emplaced in the upper crust prior to eruption and solidification, respectively. The crystal-poor Chayano-Ebisutoge rhyolite (>100 km^3 DRE) is compositionally distinct from the Nyukawa and Takidani magmas and its generation is associated with a substantial contribution of crustal melts. Yet, plagioclase and orthopyroxene textures and chemistry provide strong evidence that the ascending rhyolite percolated through the upper Takidani-Nyukawa mush zone prior to eruption. Overgrowth of "rhyolitic plagioclase" on "xenocrystic dacitic plagioclase" typical of the Takidani-Nyukawa magmas indicates that the extraction and accumulation of the rhyolitic melts could have occurred in less than 10 kyr (i.e. time between eruptions) prior to eruption providing maximum timescales for pre-eruption storage. Overall, our findings show a progressive growth and thermal maturation of a vertically extended magmatic plumbing system over hundreds of thousands of years and imply that large volcanic eruptions can occur in relatively short succession without dramatic changes in

the plumbing system, thus, complicating the identification of signs of an impending large eruption.

INTRODUCTION

The relationship between volcanic and plutonic rocks holds important information about the chemical differentiation of magmas and generation and timescales of some of the largest eruptions on Earth. The chemical differentiation of magma is a fundamental igneous process that contributes to the construction of the Earth's crust and leads to a variety of volcanic eruptions. According to our current views magma differentiation takes place in transcrustal magmatic systems that consist of vertically connected magma reservoirs (Lipman 1984; Hildreth 2004; Marsh 2004; Bachmann and Bergantz 2008; Cashman et al. 2017; Jackson et al. 2018; Sparks et al. 2019; and references therein). Geochronological studies show that magmatic systems can be long-lived and grow incrementally over hundreds of thousands to millions of years (Coleman *et al.*, 2004; Deering *et al.*, 2016). Petrological studies further suggest that magma reservoirs are dominated by magma mushes, porous frameworks of crystals that hold melt and magmatic volatiles in the pore spaces (Cashman *et al.*, 2017; Paulatto *et al.*, 2019; Sparks *et al.*, 2019). Within the mush columns segregation of residual melt can lead to the formation of voluminous melt-rich lenses (i.e. liquid-filled magma chambers), which, once developed, are thought to be ephemeral features of long-lived magmatic systems (Hartung *et al.*, 2017; Gualda *et al.*, 2018; Floess *et al.*, 2019; Paulatto *et al.*, 2019).

Storage of highly differentiated magma appears to predominantly occur in the upper continental crust (<10 km, Gualda et al. 2018). Numerical models that incorporate the physical parameters of magma, on the other hand, demonstrate that magma differentiation is volumetrically and thermally favoured in the middle and lower crust (Dufek and Bergantz,

2005; Annen *et al.*, 2006). If differentiation dominantly takes place at greater depth, effective mechanisms are required that separate chemically differentiated melt from the crystal mush and subsequently transport the silicic and viscous melt through the transcrustal mush columns (e.g. Ducea *et al.*, 2017; Bachmann and Huber, 2019; Karakas *et al.*, 2019; Sparks *et al.*, 2019). Hindered crystal settling and compaction are thought to play a dominant role in the phase separation process at high crystal fractions (McKenzie, 1984; Miller *et al.*, 1988; Bachmann and Bergantz, 2004; Dufek and Bachmann, 2010; Lee *et al.*, 2015; Holness, 2018). Additional, but less-well constrained, drivers of efficient phase separation include gas-filter pressing, deformation-induced segregation, shearing and vibro-agitation of magma reservoirs (Anderson *et al.*, 1984; Rutter and Neumann, 1995; Vigneresse *et al.*, 1996; Sisson and Bacon, 1999; Petford *et al.*, 2000, 2020; Davis *et al.*, 2007; Kohlstedt and Holtzman, 2009; Pistone *et al.*, 2015). However, the mechanism leading to phase separation and magma differentiation and associated timescales remain poorly constrained.

The rates at which melt can be extracted strongly depend on the permeability of the magma body and the viscosity of the melt. The extraction and accumulation of melt can occur over a range of timescales and can arguably vary between months to centuries (Druitt *et al.*, 2012; Gualda *et al.*, 2012b; Barker *et al.*, 2016) to millennia of years (Bachmann and Bergantz, 2004). The wide range in timescales and lack of petrological constraints complicates interpretations of geophysical data of active systems making any prediction of imminent large silicic eruptions challenging, if not impossible.

Evidence for large-scale extraction processes is commonly drawn from volcanic sequences (i.e. crystal-poor rhyolites) in systems where fractional crystallisation appears to control magma evolution (Bowen, 1928). Granitoids of intermediate composition are in some cases considered as the solidified magma reservoirs that hold the crystal residues (or cumulates) left behind after extraction and eruption of the interstitial rhyolitic melt (Bachl *et*

al., 2001; Bachmann and Bergantz, 2004; Lowery Claiborne *et al.*, 2006; Deering and Bachmann, 2010; Gelman *et al.*, 2014; Lee and Morton, 2015; Lipman and Bachmann, 2015; Deering *et al.*, 2016; Fiedrich *et al.*, 2017; Schaen *et al.*, 2017), and hold textural records of melt extraction processes. Identifying the restricted conditions conducive to large explosive silicic eruptions, however, remains difficult because the lack of coexisting plutons and volcanic deposits reduces our capacity to trace magmatic processes and timescales prior to large volcanic eruptions (Bowen, 1928; Hildreth, 1981; Bachmann and Bergantz, 2004; Glazner *et al.*, 2008; Dufek and Bachmann, 2010; Schaen *et al.*, 2017).

In central Japan, we have the unique opportunity to examine a section through a nearly 2 km thick shallow intrusion (the Takidani pluton; Fig. 1; Harayama 1992; Hartung et al. 2017), which based on spatial and temporal constraints is recognised as the exhumed magma reservoir that fed two of the largest eruptions in Central Japan in the Late Pleistocene. The proximal deposits of these eruptions include the 1.76 Ma Nyukawa Pyroclastic Flow Deposit and approximately 10 kyr younger Chayano Tuff and Ebisutoge Pyroclastic Deposits (Nagahashi 1995; Yoshikawa et al. 1996; Harayama 1998, 1999; Nagahashi et al. 2000). In this contribution, we aim to explore the relationships between the volcanic and plutonic units using major and trace element chemistry of whole-rock, minerals and glass (1) to reconstruct the architecture of the magmatic plumbing system, (2) to identify the magmatic processes leading up to the caldera-forming eruptions in the Northern Japan Alps, and (3) to establish relationships between volcanic and plutonic systems.

GEOLOGICAL BACKGROUND

The Hida mountains and Norikura Volcanic Chain

The Hida mountains form the Northern Japan Alps in Central Honshu along the eastern margin of the Eurasian plate. They are located within a convergent tectonic setting and have

been rapidly uplifted and denudated following the E-W compression of the North American and Eurasian plates as result of the subduction of the Pacific and Philippine Sea plates. The Hida basement rocks form the thickest crust in Japan with a thickness of about 35 km (Zhao et al., 1992), and comprise Mesozoic metamorphic rocks, Cretaceous accretionary complexes and Cretaceous to Paleogene plutons and volcanic units (Yamada, 1977; Yamada and Kobayashi, 1988; Harayama, 1990; Harayama et al., 1991). The Norikura Volcanic Chain formed along the crest of the Northern Japan Alps at about 2.7 Ma and include the Ueno Basalts, the Nomugi-toge Volcanic Rocks, and the Hida Volcanic Rocks. The Ueno Basalts and the Nomugi-Toge andesitic rocks were erupted over ca. 1 Ma until 1.5 Ma (Kimura and Yoshida, 1999; Kimura *et al.*, 2002). The Nyukawa Pyroclastic Flow Deposit and Chayano Tuff and Ebisutoge Pyroclastic Deposit erupted near the Plio-Pleistocene boundary at 1.75-1.76 Ma. At ca. 1.3 Ma, new volcanic centres started to develop including Ontake, Norikura, Yake-dake, Washiba-Kumono-taira, Tateyama and Shirouma-oike (Kimura and Yoshida, 1999). Ontake and Yake-dake volcanoes erupted in recent years.

The Takidani pluton

The Takidani pluton (TK) is one of the youngest exhumed granitic intrusions on Earth (1.1-1.6 Ma; Ma; Harayama 1992; Sano et al. 2002; Ito et al. 2017; Farina et al. 2020). It is located in the Hida Mountains in Central Japan between Okuhotaka-dake and the active Yake-dake volcano (Fig. 1a-b, 2a-c; last eruption 1995; Global Volcanism Program 1995). The pluton intruded at the base of the Hotaka Andesite, a caldera fill sequence of co-genetic tuffs, lavas and porphyritic sills (Harayama, 1990, 1999). The rapid uplift and denudation of the Hida Mountains (Harayama *et al.*, 1991; Harayama, 1992; Yamada, 1999; Sueoka *et al.*, 2016; King *et al.*, 2020) led to high exhumation rates (5.1-7.5 mm yr^{-1}, Bando et al. 2003) and eastward tilting of this volcanic-plutonic complex and to the vertical exposure of the

nearly 3 km thick caldera infill and 2 km thick section of the sub-volcanic intrusion (Fig. 1c; Harayama et al. 2003).

The TK comprises at least six texturally and chemically distinct lithological units of granodiorite and granite (Table 1; Fig. 3). All units contain plagioclase, quartz, alkali feldspar, hornblende and/or biotite and iron oxides in varying amounts (Bando *et al.*, 2003; Hartung *et al.*, 2017). Apatite (0.2-0.3 area%), titanite (0.1-0.3%) and zircon (0.02%) are common accessory phases. Orthopyroxene is recorded in trace amounts (Bando *et al.*, 2003; Hartung *et al.*, 2017). The top unit in contact with the caldera fill is a medium-grained porphyritic phenocryst-dominated granodiorite (mGT; marginal granodiorite; Fig. 3a) and marked by reversely zoned plagioclase and reaction rims of biotite (Hartung *et al.*, 2017). In the Nishiho-zawa valley, the mGT is underlain by an isolated unit of fine-grained porphyritic granite (fGT2; Fig. 3b; supplementary data S1). In the Shiradashi-zawa valley, the mGT is followed by fine-grained porphyritic matrix-dominated granodiorite and low-silica granite (pGT, Fig. 3c) and medium-grained equigranular hornblende-biotite granodiorite (GDT, Fig. 3d). A gradual transition in texture from medium-grained equigranular to fine-grained porphyritic granodiorite and gradual enrichment in silica content is observed from the GDT to the pGT units (Hartung *et al.*, 2017). This textural transition is accompanied by an increase in the fraction of quartz and feldspars from 50 to 70 area%, and is interpreted to have resulted from upwards melt segregation and accumulation followed by rapid decompression associated with eruptive activity (Hartung *et al.*, 2017, 2019). The middle section and most voluminous unit of the Takidani pluton consists of medium-grained equigranular granodiorite (GRT; Fig. 3e), that can be distinguished from the GDT by its grey-pinkish color and lower content of mafic minerals. Towards the bottom, GDT shows progressive replacement of amphibole to biotite and iron oxides (Hartung *et al.*, 2017). The basal and deepest exposed unit of the pluton is a fine-to-medium grained biotite granite (fGT1; Fig. 3f) that is marked by

complete alteration of amphibole to biotite and iron oxides. Decimetre- to metre-scale mafic intrusions are found at the base of the pluton in the fGT1 unit and in large boulders in the Shiradashi-zawa river valley (Fig. 2d). Centimetre- to decimetre-scale ellipsoidal mafic magmatic enclaves (MME) locally exist throughout the pluton, however, most are observed in river boulders. Small cross-cutting aplitic dikes of less than 20 cm and local melt segregation features are present throughout the pluton (Fig. 2e). Detailed petrographic descriptions of the lithological units (with exception of fGT2) are provided by Hartung et al. (2017). Descriptions of the fGT2, mafic magmatic enclaves, aplitic dikes and melt segregation are available in the online supplementary material (i.e. S1).

First U-Pb ages of zircon using an ion microprobe were reported by Sano et al. (2002) and yield simple and total isochron ages of 1.36 Ma and 1.54 Ma (± 0.23 Ma), respectively. More recently, disequilibrium-corrected U-Pb zircon ages were obtained using LA-ICPMS (laser ablation inductively coupled plasma mass spectrometry) for one sample from the south-eastern part of the pluton giving a weighted mean of 1.58 Ma (± 0.1 Ma; Ito et al. 2017). Farina et al. (2020, 2021) report new U-Pb zircon ages for the mGT, pGT and GDT units (e.g. melt segregation units in the upper section) in the range of 1.2 to 1.5 Ma using CA-ID-TIMS (chemical abrasion isotope dilution thermal ionisation mass spectrometry) and in the range of 1.1 to 1.6 Ma using in-situ SIMS (secondary ion mass spectrometry). The analysed units show variable but overlapping zircon ages. A spread in zircon crystallisation age is recorded for each unit in the order of 100 to 350 kyr. Together, the U-Pb zircon ages of the TK provide a record of crystallisation from ca. 1.6 to 1.1 Ma.

The Volcanic Units

The Hotaka Andesite (caldera fill deposit)

The Hotaka Andesite (HA; Fig. 1; 1.76 Ma; Harayama 1998, 1999) is located in the in the Hida Mountains below Okuhotaka-dake (i.e. 3190 m; Fig. 2b), and sits directly on top of the TK. The HA comprises andesitic to dacitic welded tuff sheets and subordinate lavas, collapse breccias, granophyric dikes and porphyritic sills of up to 3 km thickness (Harayama, 1990) that were deposited inside a north-south oriented graben (Harayama, 1992). The welded tuff sheets of the HA were intruded by porphyry dikes and contact metamorphosed to hornblende and biotite hornfels facies by the intrusion of the TK (Harayama, 1990, 1992). The HA contains plagioclase, orthopyroxene, clinopyroxene and iron oxides (45-60 vol%, Pl>Opx>Cpx<Oxides; Harayama 1990). The age of the HA was originally reported at ca. 2.4 Ma using zircon fission track methods (Harayama, 1990, 1992). Correlation with widespread marker ash beds (i.e. Kd39; Nagahashi et al. 1996, 2000) and new zircon fission track ages of an outflow facies of HA led to a revised age constraint and an eruption age of 1.76 Ma (± 0.17 Ma; Harayama 1998).

The Nyukawa dacite (caldera outflow deposit)

The Nyukawa Pyroclastic Flow Deposit (NPFD) is a welded dacite ignimbrite of up to 100 m thickness (Fig. 4a-c; Nagahashi 1995; Nagahashi et al. 2000; Kimura and Nagahashi 2007) exposed in the Takayama area (Fig. 1a) and Matsumoto basin. Its erupted volume has been estimated to exceed 400 km^3 dense rock equivalent (DRE; Oikawa 2003). The spatial distribution of correlated tephra beds (i.e. Kd39) point towards an eruption centre in the Northern Japan Alps near Okuhotaka-dake (Nagahashi et al. 2000; Kataoka et al. 2001). The composition and mineral assemblages of the NPFD and the HA (i.e. caldera fill sequence below Okuhotaka-dake) are similar, therefore, the NPFD has been regarded as an outflow

phase of the Hotaka Cauldron that also produced the HA (Harayama, 1990). The eruption age of NPFD is estimated at 1.76 Ma (± 0.17 Ma; Harayama 1998) using fission track methods. Harayama (1998) dated the Takagariyama-I Tuff, which was correlated with the NPFD by Nagahashi et al. (1996). Farina et al. (2021) record a U-Pb zircon crystallisation age of 1.706 ± 0.087 Ma using high-precision U-Pb zircon dating by CA-ID-TIMS, consistent with published fission track ages. The NPFD contains about 30 to 40 vol.% crystals including plagioclase, orthopyroxene, clinopyroxene (Kimura and Nagahashi, 2007), iron oxides and small amounts of quartz and amphibole. Zircon and apatite are common accessory phases.

The Chayano-Ebisutoge rhyolite

The Chayano Tuff (CT) and Ebisutoge Pyroclastic Deposit (EPD) are a sequence of rhyolitic voluminous ash fall and pyroclastic flow deposits (Fig. 4a,d,e; Nagahashi 1995). They have a combined estimated eruptive volume of 380 to 490 km^3 (Nagahashi *et al.*, 2000; Kimura and Nagahashi, 2007) with a DRE of >100 km^3 (Kataoka *et al.*, 2001). The proximal deposits of the rhyolitic eruptions consist of pyroclastic flow deposits located in the Takayama Basin (L1, Fig. 1a, 4e) and Matsumoto area. The rhyolite sequence sits on top of the NPFD (Nagahashi *et al.*, 2000; Kataoka *et al.*, 2001). The distal ash fall deposits of the CT and EPD are widespread marker beds that are distributed over hundreds of kilometre across central Honshu and are described as the Kd38 volcanic ash (Unit A1 to B; Yoshikawa et al. 1996; Nagahashi et al. 2000; Kataoka et al. 2001). The age of the rhyolite eruptions is constrained through the magnetostratigraphic location of the Kd38 (i.e. CT-EPD) and the Kd39 (i.e. NPFD) tephra layers in marine sediments, which suggests that the crystal-poor rhyolites erupted approximately 10 kyr after the crystal-rich dacite at about 1.75 Ma (Yoshikawa *et al.*, 1996; Harayama, 1998, 1999). The overlapping spatial distribution of the distal tephra layers indicates that the rhyolites of the CT-EPD were erupted from the same or nearby location as

the NPFD (Nagahashi *et al.*, 2000). However, the exact eruption source of the rhyolite eruption remains unclear because of the rapid uplift and denudation of the Hida Mountains and associated erosion of the proximal fall deposits (Harayama *et al.*, 1991; Harayama, 1992; Yamada, 1999; Sueoka *et al.*, 2016; King *et al.*, 2020).

The CT comprises pyroclastic fall and non-welded flow deposits of up to 4 m thickness (Fig. 4a,e) that contain plagioclase (0.03), quartz (0.01) and traces of iron oxides, hornblende, orthopyroxene, clinopyroxene, biotite and zircon (Nagahashi *et al.*, 2000). Nagahashi (1995) has divided the EPD into four main units: Unit-A, a 20 cm thick pumice fall out containing small amounts of lithics; Unit-B, an approximately 10 m thick unconsolidated flow unit containing pumice and lithics; Unit-C, a 10 to 20 cm thick pumice fall out containing small amounts of lithics; and Unit-D, a >30 m thick welded ignimbrite with fiamme (Fig. 4a,d,e; Nagahashi et al. 2000). With an estimated 250 to 350 km^3 Unit D presents the most voluminous portion of the EPD (Kataoka *et al.*, 2001). The EPD is characterised by the abundance of plagioclase (0.03) and traces of quartz, iron oxides (magnetite and ilmenite), orthopyroxene, amphibole, biotite, quartz and zircon (Table 2; Nagahashi 1995; Nagahashi et al. 2000). Yoshikawa et al. (1996) and Nagahashi et al. (2000) also record traces of clinopyroxene. Clinopyroxene was not observed in this study. Detailed stratigraphic descriptions and mineral fractions of the proximal and distal deposits of the CT and EPD are provided in Nagahashi et al. (2000), Kataoka et al. (2001) and references therein. Chemical and mineralogical data are available from Kimura and Nagahashi (2007).

METHODS

Material and sample locations

Rock samples of the TK and HA were collected from outcrops from West-East trending river valleys called Takidani, Shirasashi-zawa, Nishiho-zawa and Yanagi-dani, and from the

Nishiho-track between the Nishihodakaguchi Station and mountain peak of Nishihotaka-dake (Fig. 1b). Samples of the TK and HA are very fresh and show little or no sign of hydrothermal alteration. Additional loose rock samples of the different lithological units of the TK and HA were also collected and analysed but are not included in the figures. All analyses are provided in the online supplementary material (i.e. S1-S3). Aplitic dikes were sampled from outcrops in the Shiradashi-zawa (i.e. EH13, EH22) and Takidani valleys (i.e. EH45). Loose rock samples containing aplitic veins were also collected from boulders in the Shiradashi-zawa valley and along the Nishiho-track. Veins were separated from the host rock and analysed individually. A variety of mafic magmatic enclaves were collected from boulders in the lower Shiradashi-zawa valley (i.e. EH80A-R) and along the Nishiho-track (i.e. EH49A-56C). Two samples were collected from outcrops at the western margin of the pluton in the Yanagi-dani valley (i.e. EH25A, EH25E).

The NPFD and EPD (i.e. Unit B to D) were sampled at three different locations in the Takayama area (L1-3; Fig. 1a). We collected four samples of the NPFD. Due to alteration and high loss on ignition (LOI) only two samples (i.e. EH61, EH62) are presented and discussed here together with published data. Whole-rock data of the two omitted samples (i.e. EH60A-B) are provided in the online supplementary material (i.e. S3). Seven samples were collected from the EPD. Individual pumices were picked from Units B (i.e. EH63) and Unit C (i.e. EH64), while bulk samples were collected for Unit D (i.e. EH65A-D). Samples of the CT were in poor condition and not suitable for major and trace element analyses.

Whole-rock analyses

Major element compositions were measured using a PANalytical AXIOS MAX X-ray fluorescence (XRF) set up with a Rhodium anode tube at 4 W at the University of Lausanne. SY-2, BHVO, JCH-1, NIM-N and NIM-G standards were used for quality control. Trace

element concentrations were measured on the same glass beads by laser ablation inductively coupled plasma mass spectrometry (LA-ICP-MS) using a Quadrupole spectrometer Agilent 7700 interfaced to a GeoLas 200M 193 nm excimer ablation system at the University of Lausanne. The system was operating at 1420 W with a laser repetition rate of 10 Hz and a 120 µm spot size. Each sample was measured at three locations for ca. 60 s (i.e. peak measurements). The background was measured for 90 s before the three ablations. For each set of five sample analyses two analyses of the NIST SRM 612 standard were performed before the first and after the last spot analysis. Trace element concentrations were recalculated using the CaO contents from XRF analyses and NIST SRM 612 as external standards. Data reduction was performed using the LAMTrace software package (Jackson *et al.*, 1992; Longerich *et al.*, 1996; Jackson, 2008a, 2008b). Measurement precision and all whole-rock major and trace element compositions (i.e. raw and normalised values) are provided in the online supplementary material (i.e. S2, S3).

Glass and mineral analyses

Major and minor element analyses of minerals and glasses were performed on 100 µm thick thin sections using a JEOL 8200 Superprobe electron probe micro-analyser (EPMA) at the University of Geneva. The microprobe is equipped with a five-channel wavelength-dispersive spectroscope system (WDS) and was operated at an accelerating voltage of 15 keV and a beam current of 15 nA for plagioclase, pyroxene and amphibole analysis, 15 keV and 20 nA for oxide analysis and 20 keV and 2 nA for glass analysis. A defocused beam of 2 µm diameter was used for plagioclase, pyroxene and amphibole analysis. Oxides were analysed with a focussed beam diameter of <1 µm. Only analyses with a maximum error of 1% were retained and cross checked by recalculating the appropriate mineral formula. Matrix glass was analysed in pumices and fiamme with a defocused beam of 10 µm. Plagioclase crystals

were analysed on core-to-rim profiles. Eighteen crystals were chosen for trace element analyses: nine from the TK, three from the NPFD and six from the EPD (i.e. online supplementary material S3, S4).

Trace element concentrations in plagioclase were measured with LA-ICP-MS using a sector-field spectrometer Element XR interfaced to a NewWave UP-193 ArF excimer ablation system at the University of Lausanne. The system was operating at 1400 W with a laser repetition rate of 20 Hz. The spot size ranged between 25 µm (i.e. high-An cores) and 100 µm for plagioclase analysis. Standards were analysed with a spot size of 75 µm. For each spot analysis, the background was first measured for 30 s before ablation and peak measurement of 60 s each. Trace element concentrations were recalculated using CaO contents of plagioclase from EPMA analyses as internal standard and NIST SRM 612 as external standard. Data reduction was performed using the LAMTrace software package (Jackson *et al.*, 1992; Longerich *et al.*, 1996; Jackson, 2008a, 2008b). Measurement precision and glass and mineral analyses are provided in the online supplementary material (i.e. S2, S3).

GEOCHEMISTRY

Whole-rock geochemistry

The whole-rock compositions of the TK and the volcanic units are generally sub-alkaline and range from andesite and dacite to rhyolite compositions (Fig. 5). Magmatic enclaves found in the TK units extend from the field of sub-alkaline compositions (i.e. andesite) into the field of mildly-alkaline lavas (i.e. basaltic trachy-andesite and trachy-andesite) and have silica contents between 54 to 62 wt.% SiO_2 (Fig. 5, 6). Compositions of the main lithologies of the TK range from 64 to 76 wt.% SiO_2 comprising granodiorite and high-silica granite. Aplitic dikes cross cutting the pluton form a high-silica endmember (up to 78 wt.%). The NPFD and HA are dacitic in composition with silica contents between 62 to 68 wt.% SiO_2 (including

data from Kimura and Nagahashi 2007) and 63 to 65 wt.% SiO_2, respectively. Analyses of pumices and bulk samples of the EPD (i.e. Units B and D) reveal relatively similar silica contents of about 73 to 74 wt.% (i.e. anhydrous) and are consistent with published analyses of pumices of the EPD (Fig. 5, 6; Kimura and Nagahashi 2007). Sample EH65A (i.e. base of Unit D) is less chemically evolved with about 71 wt.% SiO_2 (i.e. anhydrous; Fig. 5,6), but it has a very high LOI (4.6 wt.%) compared to the rest of Unit D (ca. 2 wt.%).

A decrease with increasing silica content is observed for Al_2O_3 (18-12 wt.%), TiO_2 (1.4-0.1 wt.%), Fe_2O_3 (9.3-0.5 wt.%), MgO (4.5-0.02 wt.%), MnO (0.25-0.01) and CaO contents (8.2-0.5 wt.%) (Fig. 6a-f). Rhyolite samples of the CT and EPD have higher Al_2O_3 and MnO contents (Fig. 6a,e) and lower TiO_2, MgO and CaO contents compared to the plutonic samples (Fig. 6b,d,f). Parallel trends of Na_2O vs SiO_2 contents are observed for the plutonic and volcanic rocks (Fig. 6g) with the NPFD, CT and EPD generally containing about 1 wt.% less Na_2O than samples of the TK. The volcanic and plutonic units generally overlap in K_2O content and show a gradual enrichment in K_2O content from 1.6 to 6.2 wt.% (Kimura and Nagahashi, 2007) with increasing silica content (Fig. 6h). The EPD rhyolite plots in two distinct groups on Na_2O and K_2O variation diagrams: Unit B (i.e. pumices from unconsolidated pumice flow deposit) plots together with published pumice analyses of Kimura and Nagahashi (2007). Unit D (i.e. bulk analyses of the welded ignimbrite), on the other hand, shows relatively lower and higher Na_2O and K_2O contents, respectively, similar to TK granite (Fig. 6g,h). The concentrations of Rb gradually increases with increasing silica content starting at about 60 wt.% SiO_2 from about 50 to 200 ppm displaying a similar trend to K_2O contents (Fig. 6h,i). Rb concentrations in magmatic enclaves vary between 60 and 230 ppm with no clear trend (Fig. 6i). The amount of Sr initially increases with increasing silica content from about 200 to 530 ppm in the enclaves of the TK but decreases with increasing silica content in the plutonic and volcanic units from about 400 to 50 ppm (Fig. 6j). Glass

analyses of the NPFD of Kimura and Nagahashi (2007) contain about twice as much Sr as matrix glass of the CT and EPD (Fig. 6j). Barium generally behaves incompatibly with concentrations reaching nearly 1000 ppm in the volcanic glass (Fig. 6k). A strong decrease in Ba content with increasing silica content from 375 to 36 ppm is observed in aplitic dikes (Fig. 6k). The volcanic units are relatively enriched in Ba compared to plutonic rocks. Concentrations of Zr are distributed over a M-shaped pattern with no clear trends for volcanic and plutonic rocks (Fig. 6l). The volcanic units generally contain higher concentrations of Zr than the plutonic counterparts. Rhyolite samples plot in a distinct group on a Ba-Sr and Zr-Nb variation diagrams (Fig. 6m,n). Trace element variations between the NPFD and HA samples are apparent in Zr-Nb and Ba-Sr plots (Fig. 6l,n).

Trace element variations are shown in Figure 7 for the plutonic and volcanic units and are similar for both granite and granodiorite samples of the TK (Fig. 7a). However, the granite samples display more pronounced negative Sr and Eu anomalies and are slightly enriched in Th and U and in heavy rare earth elements (HREE; Fig. 7a). The aplitic dikes are strongly depleted in the middle and HREE with some displaying a clear “spoon-shaped” pattern. Magmatic enclaves, contrastingly, are relatively depleted in Th and U and strongly enriched in HREE (Fig. 7a). Rhyolite and dacite samples have similar trace element patterns (Fig. 7b). Rhyolite samples show more pronounced Sr and Eu anomalies and are relatively enriched in HREE compared to dacitic samples. The REE patterns of the NPFD and HA overlap with the samples of granodiorite of the TK (Fig. 7c). Different to TK and NPFD samples, HA samples show a slight positive Eu anomaly. The rhyolite samples of the CT and EPD show comparable trends to the granite samples of the TK (Fig. 7d). Overall, the rhyolite samples have higher REE concentrations and overlap just marginally with the granite units (Fig. 7d).

Pumice and glass chemistry

We present new major and minor element data of glass shards of Units B, C and D of the EPD. Our analyses are generally in agreement with published data of Kimura and Nagahashi (2007), with silica contents ranging between 76.6 and 76.9 wt.% SiO_2 (Fig. 5,6). MgO contents are strongly depleted in the EPD and CT samples showing mean and maximum values of 0.03 and 0.15 wt.%, respectively (Fig. 6b). The K_2O contents span from 4.2 to 5.0 wt.% K_2O (i.e. anhydrous) and are in good agreement with published data (Fig. 6d; Kimura and Nagahashi 2007). However, a disparity exists between our results and existing Na_2O values. The Na_2O contents from this study vary between 3.4 and 3.9 wt.%, and on average are about 0.7 wt.% higher than the published data (Fig. 6c). The analytical conditions for glass analyses are not reported in Kimura and Nagahashi (2007). To ensure the accuracy of our analyses we decreased the beam current to 2 nA and increased the beam size to 10 µm after standard calibration. We also monitored the measurements of counts-per-second on the peak position to ensure there was no significant loss of sodium. Trace element data of Kimura and Nagahashi (2007) record negative Eu and Sr anomalies of the CT and EPD glasses and an enrichment in HREE with respect to whole-rock compositions of the NPFD, HA and TK (Fig. 7).

MINERAL COMPOSITION

Iron oxides

Magnetite and ilmenite grains that are adjacent and in direct contact are commonly observed in the NPFD (Fig. 4c, 8a). Both magnetite and ilmenite are present in the EPD but rarely found as adjacent grains. Oxide compositions in the NPFD are generally characterised by low TiO_2 contents and high Fe_2O_3-FeO ratios (supplementary data files). In comparison, oxides of the EPD are relatively enriched in TiO_2 and MnO contents and depleted in MgO content.

Magnetite in the TK overall contains less TiO_2 and MnO with respect to the NPFD and EPD (Hartung *et al.*, 2017). Oxygen fugacity calculated from the compositions of oxides from the NPFD indicate values at or slightly above the nickel-nickel-oxide buffer (NNO, Fig. 9). Calculations for magnetite and ilmenite (adjacent pairs and non-adjacent crystals) indicate more reduced conditions for the rhyolite samples of the EPD at about 1 to 2 log units below NNO (Fig. 9; Kimura and Nagahashi 2007). Temperature estimates based on Fe-Ti exchange (Fig. 9; Ghiorso and Evans 2008) range between 820°C and 920°C in the NPFD, and between 720°C and 790°C in the EPD (Kimura and Nagahashi 2007). The first unit of the CT records a high magmatic temperature and oxygen fugacity similar to the NPFD (Fig. 9; Kimura and Nagahashi 2007).

Pyroxene

Orthopyroxene is abundant in all volcanic units and usually occurs as subhedral crystals (Fig. 8b-d). Analyses are generally consistent with compositions reported by Kimura and Nagahashi (2007). Orthopyroxene in the NPFD is Mg-rich ($Mg\#_{61-58}$; Fig. 8c, 10), whereas, in the EPD, orthopyroxene is generally Fe-rich ($Mg\#_{35-28}$; Fig. 8b,d,10). However, we found traces of Mg-rich orthopyroxene in Unit D of the EPD similar in composition to NPFD orthopyroxene (Fig. 8d). Clinopyroxene with Mg numbers of around 70 are reported by Kimura and Nagahashi (2007) (Fig. 10). Clinopyroxene was neither observed in the NPFD nor in analysed samples of the EPD.

Amphibole

Anhedral Fe-rich amphibole inclusions ($Mg\#_{40-36}$; Fig. 8b, 10), characteristic of high Al_2O_3 and low CaO content, locally exist in orthopyroxene crystals in Unit D of the EPD. Similar compositions are reported as clinopyroxene in Kimura and Nagahashi (2007). Amphibole

inclusions are ferro-hornblende in composition (Leake et al. 1997). Amphibole compositions of the TK are bimodal and span from magnesio-hornblende to actinolite and are reported in Hartung et al. (2017).

Plagioclase

Plagioclase is the dominant mineral phase in both the volcanic and plutonic units. We analysed major and trace element concentrations along core-to-rim transects including nine plagioclase crystals from the TK, three crystals from the NPFD and six crystals from the EPD. Chemical profiles of representative plagioclase are shown in Figure 11. Plagioclase phenocrysts in the TK units show the biggest range in composition and overall vary from 90 to 30 mol% Anorthite (An). Three distinct plagioclase populations are identified by Hartung et al. (2017) based on the main growth zone. All plagioclase crystals contain a main growth zone of ca. 30 to 60 mol% An content, that displays oscillatory zoning, and a sodic rim of 30 to 15 mol% An content of varying thickness (Hartung *et al.*, 2017). Some plagioclase crystals also contain high-An cores. The FeO content of the TK plagioclase generally ranges between 0.4 and 0.2 wt.% and decreases to about 0.1 wt.% FeO in the outer rim (Fig. 11,12; Hartung et al. 2017). Plagioclase rims are depleted in Sr, Ba and REE concentrations compared to core and mantle plagioclase compositions of the TK (Fig. 11-13).

The NPFD contains subhedral plagioclase with An contents varying between 38 and 60 mol% (Fig. 11,12). Crystals are characterised by oscillatory zoning ($An_{40–50}$) and locally high-An zones of up to 60 mol%. A rimward increase in An content of about 5 mol% is accompanied by an increase in FeO content from about 0.3 to 0.4 wt.%. All analysed plagioclase phenocrysts have a common rim composition of about 40 to 45 mol% An content with similar trace element concentrations (Fig. 12). Plagioclase grains in the NPFD are texturally and chemically comparable to cores and mantles of the TK (Fig. 11-13).

Plagioclase in the EPD is present as euhedral to subhedral laths of up to 2 mm length. The An content varies between 27 and 43 mol%, which is in agreement with published data of Kimura and Nagahashi (2007). Some crystals contain resorbed Albite-rich cores (An_{30}) that are overgrown by a more calcic band (Fig. 11). The outer rims of plagioclase in the EPD are homogeneous and are sodium rich with An contents of 28 to 30 mol%. Finely-spaced oscillatory zoning of 1 mol% An content is a common feature of all crystals. Concentrations of Sr increase with increasing An content while Ba, La, Ce and Pb concentrations decrease and FeO content remains relatively unchanged (Fig. 11, 12). Rim compositions are depleted in Sr and Ba. Locally, xenocrystic cores exist in the EPD plagioclase that are texturally and chemically distinct from the main growth (Fig. 11-13). Most xenocrystic cores are subhedral and have An contents of about 40 to 50 mol% (Fig. 11), while some are anhedral with An contents of ca. 30 mol%. Plagioclase composition of the EPD differ distinctively from plagioclase of the TK and NPFD displaying high Sr and Eu concentrations (Fig. 12b, c). The texture and composition of the subhedral high-An xenocrystic cores are comparable to the plagioclase compositions of the GRT unit of the TK (Fig. 13d).

Rhyolite-MELTS barometry

We used the rhyolite-MELTS (Version 1.1.0; Gualda et al. 2012a; Ghiorso and Gualda 2015) barometer to calculate the equilibration pressures of melt, quartz and 1 or 2 feldspars in P-T space and estimate the extraction and storage conditions of the crystal-poor rhyolites (Gualda and Ghiorso, 2014; Gualda *et al.*, 2019). In haplogranitic/rhyolitic systems, the cotectic between quartz and feldspars shifts towards quartz with decreasing pressure (Johannes and Holtz, 1996). The rhyolite-MELTS geobarometer uses the composition of the matrix (or the whole rock) to determine at which pressure the difference in saturation temperature for quartz and 1 or 2 feldspars (i.e. plagioclase and/or alkali feldspar) is the

smallest. The pressure at which the difference in liquidus temperatures are identical or smallest, best corresponds to the extraction (i.e. whole-rock; Gualda et al. 2019) or pre-eruptive storage pressure of rhyolitic magma (i.e. matrix glass; Gualda and Ghiorso 2014). As the composition of the liquid (i.e. matrix glass) equilibrates with the crystals during pre-eruptive storage, the rhyolite-MELTS geobarometer can be used to assess the pre-eruptive storage pressures of rhyolite magma (Gualda and Ghiorso, 2014).

As a first step, we performed multiple isobaric rhyolite-MELTS simulations from super-liquidus to near-solidus conditions using our new glass analyses of the EPD and previously reported pumice compositions of the CT and EPD (Kimura and Nagahashi, 2007). Simulations were run in 1°C steps under water-saturated conditions and repeated at pressures between 450 and 50 MPa and pressure intervals of 10 and 25 MPa for glass and pumice compositions, respectively. We determined the liquidus temperatures for quartz, plagioclase and alkali feldspar and calculated the differences in saturation temperatures between the quartz and plagioclase (i.e. quartz + 1 feldspar barometer, Q1F) and between quartz, plagioclase and alkali feldspar (i.e. quartz + 2 feldspars barometer, Q2F; Gualda and Ghiorso 2014) as a function of pressure. The pressure at which the difference between the onset of crystallisation of plagioclase, quartz and feldspar is the smallest corresponds to the best estimate of the storage pressure for matrix glass and of the extraction pressure for pumice. Pressure estimates for all glass and pumice compositions are listed in the supplementary data files and are summarised in Figure 14 for the Q1F barometer (i.e. no sanidine has been recorded in the erupted rhyolites). Pressures from glass compositions of the EPD (i.e. Unit B to D) range from 80 to 290 MPa with a peak at ca. 200 MPa (Fig.14a). Pressure estimates from pumice samples of the same units (i.e. EPD Units B to D; Kimura and Nagahashi 2007) span a range from 200 to 340 MPa and have a median value of ca. 270 MPa (Fig. 14a). An increase in pressure estimates from 150 to 340 MPa is observed for stratigraphically younger

units from the CT to Unit D of the EPD (Fig. 14b). Compositions of Unit D record the largest range in calculated pressures (Fig. 14b). Estimated errors of the rhyolite-MELTS geobarometer are about 25 MPa for the Q1F and 20 MPa for the Q2F models (Gualda and Ghiorso, 2014). Maximum errors of the rhyolite-MELTS geobarometer are based on the natural variability of Na_2O content of the Bishop Tuff and constrained at about 95 MPa for the Q1F and 43 MPa for Q2F calibrations (Gualda and Ghiorso, 2014).

We also applied the rhyolite-MELTS barometer to glass compositions of NPFD, CT and EPD of Kimura and Nagahashi (2007). Simulations yield high liquidus temperatures of quartz that do not intersect with the liquidus temperature of plagioclase and alkali feldspar which may be due to the low reported Na_2O content (Fig. 6c). The high silica content of the Nyukawa glass (i.e. 78 wt.%) is taken to imply a low pre-eruptive storage pressure, because the cotectic moves towards normative quartz with decreasing pressure (Johannes and Holtz, 1996). Kimura and Nagahashi (2007) constrain the pre-eruptive storage conditions of the NPFD at about 100 MPa by comparing the mineral assemblage of the NFPD to the water-saturated experiments of Rutherford and Devine (1996).

DISCUSSION

Petrogenesis of the intermediate and silicic compositions

Dacite and granodiorites extraction

The TK is largely composed of granodiorites that are similar in major, trace and REE compositions to the NPFD and HA (Fig. 5-7). Together with similarities in mineral chemistry between the plutonic and volcanic units and the close temporal and spatial association, these features are taken as strong evidence that the TK is petrogenetically related to the NPFD and HA. Kimura and Nagahashi (2007) propose that the TK and the NPFD are the product of large-scale upper crustal melting and magma mixing between the Ueno Basalt and the crustal

melts of older Hida granitoids (Harayama, 1990; Harayama *et al.*, 1991). The Ueno Basalt comprises alkali basalt, transitional and calc-alkaline basalts and basaltic-andesites that erupted 40 to 100 km south and south-west of the TK between 2.76 Ma and 1.34 Ma (Kimura and Yoshida 1999; Kimura et al. 2002). The cumulative eruption volume of the Ueno Basalt is relatively small (<50 km^3; Kimura and Yoshida 1999). However, Kimura and Nagahashi (2007) estimate that >300 km^3 of basaltic magma must have intruded in the upper crust to generate the erupted volumes of the NPFD (>400 km^3 dacite) and the CT-EPD (>100 km^3 rhyolite). Numerical models of magma emplacement show that substantially more basalt and heat are required to generate large volumes of silicic melts in the upper crust either by partial melting or crystal fractionation (Annen *et al.*, 2006). Yet, no evidence of such large mafic bodies has been observed in exposed crustal arcs (Jagoutz *et al.*, 2009; Jagoutz, 2014), which would support the generation of silicic melts in the lower crust where temperatures remain high (Müntener *et al.*, 2001; Dufek and Bergantz, 2005; Sisson *et al.*, 2005; Blatter *et al.*, 2013; Nandedkar *et al.*, 2014; Müntener and Ulmer, 2018). Although, the melting and mixing model of Kimura and Nagahashi (2007) may explain the isotopic variations (i.e. Nd-Sr-Pb) observed in the plutonic and volcanic rocks, it does not address the thermal limitations on upper crustal melting. In the following, we assess crystal fractionation as alternative differentiation process for generating the intermediate and silicic compositions of the TK and erupted magmas.

We model equilibrium crystallisation of the Ueno Basalt in the Takayama Basin by calculating trace and REE concentrations of the liquid fractions using partition coefficients for andesite and dacite compositions (i.e. Geochemical Earth Reference Model, online supplementary material S5). To reproduce the trace element variations of the TK, NPFD and HA about 70% of crystallisation of dominantly plagioclase and amphibole (± pyroxene) is required as well as small amounts of FeTi-oxides, apatite and zircon. The calculated mineral

assemblage is consistent with crystallisation experiments of hydrous basaltic magma at 0.7 GPa (Sisson *et al.*, 2005; Jagoutz *et al.*, 2009; Nandedkar *et al.*, 2014; Müntener and Ulmer, 2018; Ulmer *et al.*, 2018). The Ueno Basalt in the Takayama Basin (i.e. TKY1E) closest to the TK has an isotopic composition (e.g. $^{87}Sr/^{86}Sr = 0.70700$; $^{143}Nd/^{144}Nd = 0.51267$; Kimura et al. 2002) similar to the TK (e.g $^{87}Sr/^{86}Sr = 0.70676$-$0.70754$; $^{143}Nd/^{144}Nd = 0.51246$-$0.51260$; Kimura and Nagahashi 2007; Hartung et al. 2017), and indicates minor assimilation and mixing with radiogenic material supporting an evolution dominated by crystal fractionation and melt extraction processes.

The abundance of orthopyroxene in the NPFD and HA suggests that the eruptive temperature was above 800°C, which is in good agreement with temperature estimates of the NPFD from oxide thermometry (Fig. 9). Furthermore, the stabilisation of orthopyroxene indicates pre-eruptive storage in the shallow crust (<200 MPa, Andrews, 2014). The TK, on the other hand, contains amphibole instead of orthopyroxene indicating crystallisation temperatures below 800°C (Hartung et al. 2017). The NPFD and HA could have been extracted at higher temperatures and lower crystallinities and also contain less water than the TK, which would explain the slightly lower SiO_2 of the erupted units and stabilisation of orthopyroxene during storage in the shallow crust (<200 MPa, Andrews, 2014). A higher magmatic temperature could have also made the NPFD and HA more susceptible for reactivation and eruption due to its lower viscosity.

We conclude that the Takidani granodiorites and NPFD and HA dacites most likely represent extracted liquids transported from the middle to lower crust and that they are not the result of two-endmember mixing in the upper crust as previously proposed (Kimura and Nagahashi, 2007). While the hotter magmas of the NPFD and HA erupted from a transient shallow reservoir, slightly colder magmas of the reservoir solidified over hundreds of

thousands of years to form the TK in the upper crust (Harayama, 1992; Ito *et al.*, 2017; Farina *et al.*, 2020, 2021).

Granite and aplite formation

The granite units of the TK contain about 2 to 5 wt.% more SiO_2 than the most evolved granodiorite units (i.e. pGT) and about 10 wt.% more SiO_2 than the NPFD and HA (Fig. 5,6). They have very similar REE patterns to the granodiorite but are relatively depleted in Eu and Sr contents (Fig. 7a). Additional crystallisation of plagioclase and small amounts of amphibole could explain the decrease in Eu and Sr contents and REE patterns in the granite. Segregation of the interstitial granitic melt from the granodiorite and accumulation in melt rich lenses could account for major and trace element variations. Evidence for melt segregation is found in the upper section of the pluton (Hartung *et al.*, 2017) and supports that the granites were likely produced through fractional crystallisation of a granodiorite magma in the upper crust where crystallisation of plagioclase dominates (Martel *et al.*, 1999). Moreover, a lens of fine-grained granite is observed near the roof of the TK (i.e. fGT2, Fig. 1,3b). No volumetrically significant mafic magma bodies exist or have been identified within the TK, particularly within the upper part of the pluton. This suggests that the fine-grained granite unit fGT2 accumulated locally and most likely as result of phase separation processes (Bachmann and Huber, 2019). The other identified granite unit, which is the fine-to-medium grained biotite granite (fGT1, Fig. 1, 3f), is located at the base of the exposed 2 km section. If this unit is also the result of large-scale segregation, fGT1 must have been extracted from a deeper and unexposed section of the plumbing system. Pressure estimates from amphibole barometry indicates that TK magmas were emplaced at depths between 6.5 and 9.5 km (Hartung *et al.*, 2017) suggesting that extraction and emplacement of granite units occurred at shallow depth.

With up to 78 wt.% SiO_2, the aplitic dikes have the most evolved compositions of the TK. The strong depletion in Ba, Sr, Eu, Zr and Nb indicates fractionation of alkali feldspar and biotite, while the depletion in middle and heavy REE is consistent with titanite crystallisation antecedent to the aplitic melt extraction in the late crystallisation stage of the pluton (Glazner *et al.*, 2008), and supported by the abundance of titanite in the Takidani units (0.12-0.36 area%; Hartung et al. 2017).

The origin of the rhyolites

Rhyolite chemistry is significant different with respect to the compositions of granitic units of the TK. Rhyolite samples are relatively enriched in Al_2O_3 and depleted in TiO_2 and MgO (Fig. 6), which suggests that the process of formation could differ from the generation of the granite units. The Na_2O content is about 1 wt.% lower in the rhyolites than in the plutonic rocks. This depletion is also observed for the Nyukawa samples, which might indicate that a certain degree of Na-loss occurred during alteration. Glass compositions, on the hand, don't vary from plutonic samples. The rhyolites of the CT and EPD overall show little variation in major elements reflecting formation at near eutectic conditions. However, Ba and Zr concentrations are distinctively higher in rhyolite samples suggesting that these melts segregated at higher temperatures (i.e. less feldspar and zircon crystallisation) than the granitic melts. Kimura and Nagahashi (2007) show a stratigraphic decrease in SiO_2 content from the base to the top of the outcrop (L1, Fig. 1) from 75 to 73 wt.%. Glass compositions further show a decrease of K_2O and Rb contents from 4.96 to 4.20 wt.% and from 159 to 134 ppm, respectively (Fig. 6; Kimura and Nagahashi 2007). This progressive decrease illustrates relatively minor chemical zoning and might reflect increasing temperature and less fractionated magma with depth in the magma reservoir.

Two-oxide chemistry reveals oxygen fugacity and temperature estimates that are nearly 1 to 2 logs and about 100°C lower than the NPFD, respectively, with the exception of one sample of the CT (Fig. 9). The lower oxygen fugacity of the rhyolite samples is also reflected in the much higher Eu concentrations measured in plagioclase of the EPD rhyolite compared to other analysed units (Fig. 12; Aigner-Torres et al. 2007). The increased Eu content can be explained by the increase in partitioning of Eu in plagioclase with decreasing oxygen fugacity (Drake and Weill, 1975; Wilke and Behrens, 1999). Partial melting of crustal units (i.e. granitoids and metasediments) alone, as proposed by Kimura and Nagahashi (2007), may explain the isotopic and chemical signature of the rhyolite, however, the low oxygen fugacity of the rhyolitic magma, which emerges from the two-oxide and plagioclase chemistry, requires some additional explanation. As previously suggested by Kimura and Nagahashi (2007) assimilation of sedimentary units containing organic carbon could have buffered the oxygen fugacity to relatively low levels (Wyborn *et al.*, 1974; Whalen and Chappell, 1988). Resorbed Fe-rich amphibole inclusions ($Mg\#_{0.40–0.36}$; Fig. 8b, 10, supplementary data files) and resorbed albite-rich plagioclase are found in orthopyroxene crystals of the EPD rhyolites. Plagioclase phenocrysts contain resorbed Ab-rich cores that are overgrown by slightly more anorthitic plagioclase (An_{40}; Fig. 11), which could provide additional support for assimilation of crustal units. Finally, concentrations of Sr and Ba are distinctively higher and lower, respectively, in the plagioclase overgrowth (Fig. 11) suggesting recharge of hotter magma and less fractionated melt. Thus, from the mineral record we can conclude that partial melting and assimilation of country rock contributed to generating the rhyolite magmas of the CT and EPD.

Phase relationships suggest that the rhyolitic melts were stored in the shallow crust prior to eruption. Calculations from glass compositions using rhyolite-MELTS barometry (Gualda and Ghiorso, 2014) yield pre-eruptive storage pressures of 100 to 300 MPa for the

EPD that are similar to the emplacement levels of the TK (Bando *et al.*, 2003; Hartung *et al.*, 2017). No clear temperature gradient is observed in the rhyolites from oxide thermometry (Fig. 9; (Kimura and Nagahashi, 2007) supporting the application of the rhyolite-MELTS geobarometer. However, the first erupted rhyolite unit (i.e. CT Unit I; Fig. 9) records a much higher magmatic temperature than the rest of the rhyolites (i.e. CT Unit II and EPD; Fig.9; Kimura and Nagahashi 2007), which could indicate that the potentially 'hotter' rhyolite of CT Unit I is not in equilibrium with quartz and feldspar. Plagioclase compositions of Unit I of the CT also range from ca. 35 to 55 mol% An (Kimura and Nagahashi, 2007) similar to phenocryst composition of the NPFD. This could indicate that the first erupted rhyolites of the CT represent a partial or residual melt of the NPFD magma. However, it could also be an artifact. The pumice analyses of Kimura and Nagahashi (2007) used to estimate the extraction pressures of the rhyolites do not discriminate between Units I and II of the Chayano Tuff, unlike the oxide analyses used for thermometry. Thus, it remains unclear if the observed increase in extraction pressure (e.g. obtained from pumices, Fig. 14b) is the result of magma heating or if it reflects a top-to-bottom evacuation of a vertically extended magma reservoir.

Origin of mafic magmatic enclaves

Mafic magmatic enclaves (MME) are observed in most units of the TK. MME have high alkali (Fig. 5) and Rb contents (Fig. 6e) compared to the main TK units suggesting the MME and TK were derived from distinct magma sources. As discussed earlier, the chemical evolution of the TK magmas was largely driven by crystal fractionation of amphibole and plagioclase in the mid-to-lower crust. In contrast, the mildly-alkaline compositions of the MME might be better explained by decompression induced mantle upwelling (Kimura *et al.*, 2002). MME are typically fine-grained and ellipsoidal in shape (Fig. 2e, also see images in

the supplementary data files). Exchange of phenocrysts between the host magma and MME indicate mingling and local mixing of the mafic and felsic magmas. Chilled and lobate margins reflect the differences in temperature and viscosity of the two magmas. Mafic pillows are observed at the base of the pluton (e.g. Yanagi-dani) and also locally in river boulders (Fig. 2d). The pillows are surrounded by aplitic veins, which are likely the result of breakup and partial hybridisation of mafic feeder dikes during emplacement (Barbarin, 2005). Similar features are observed from the Halfmoon pluton of Stewart Island (Turnbull *et al.*, 2010) and Dinkey Creek Pluton in the San Juaquin River Canyon (Barbarin, 2005) and suggest that the TK was periodically intruded by mafic magmas.

Field and geochemical data of the MME indicate that they are not directly related to the generation of the TK. The chemical and textural features of the MME suggest that mafic magma was injected into the TK reservoir after emplacement. In areas of high crystallinity, injection occurred along fractures leading to the break-up into pillows and formation of a fine-grained texture around the pillows. In areas with lower crystallinity, injection of mafic magma resulted in the fragmentation and dispersion of the feeder dike and formation of ellipsoidal MME (Barbarin, 2005). This evidence taken together with the magma heating shown by the NPFD suggests that the upper crust was periodically intruded by mafic magma. Repeated magma influx could have contributed to facilitating melt extraction processes (Hartung *et al.*, 2017) and volcanic activity.

Linking plutonic and volcanic realms

The bulk rock chemistry of the volcanic and plutonic units indicates similar thermo-chemical evolution (Fig. 6,7), but, it does not provide conclusive evidence for their genetic link. Yet, the spatial and temporal relationships between the TK and volcanic units indicate that a

genetic link could exist. In the following, we investigate plagioclase texture and composition to establish potential genetic links between the plutonic and volcanic units.

Plagioclase chemistry is controlled by magma composition, temperature and water pressure (Housh and Luhr, 1991; Hammer and Rutherford, 2002). Most plagioclase crystals in the NPFD display compositional zoning between 39 to 51 mol% An similar to zoning in plagioclase of the TK (33-57 mol% An; Fig. 8-10). According to crystallisation experiments on dacitic magmas plagioclase compositions of the NPFD and TK (excluding rims and high-An cores) correspond to crystallinities of about 34 to 47 vol.% and temperatures of 850°C to 900°C (Costa *et al.*, 2004). This indicates that both magmas reached or were close to the rheological locking point (Marsh, 1981; Vigneresse *et al.*, 1996). Plagioclase phenocrysts of the NPFD show a rimward increase in An and FeO contents indicating progressive heating and a decreasing degree of chemical evolution of the magma in the period preceding the eruption (Ginibre *et al.*, 2002). The formation of sodium-rich rims in the TK plagioclase can be related to solidification when the magma becomes rheologically locked and melt composition heads towards the eutectic (Hartung *et al.*, 2017). Similarities in texture and compositional zoning of the main growth zone of NPFD and TK plagioclase could indicate that plagioclase phenocrysts mostly crystallised from chemically similar magmas. The different trajectories of plagioclase rim compositions of the NPFD and TK reflect different paths of the crystal-rich magmas toward reactivation and eruption and solidification, respectively (Bachmann and Bergantz, 2006; Huber *et al.*, 2010). Injection of mafic magma and partial mixing or mingling with the Nyukawa dacite could also explain some of the observed trace element variations in the NPFD (e.g. Ba, Zr; Fig. 6k,l).

Plagioclase phenocrysts of the rhyolites are chemically distinct from those of the NPFD and TK with higher Eu, Sr and Ba concentrations (Fig. 12, 13). As discussed before the relatively high Eu concentrations in plagioclase of the EPD (compared to NPFD and TK

plagioclase) are likely the result of an increase in Eu partitioning at reducing conditions (Drake and Weill, 1975; Wilke and Behrens, 1999). Higher Sr and Ba concentrations, however, indicate that EPD plagioclase crystallised from a magma source that was or became enriched in those elements (Fig. 12b,d), and that is compositionally different from the NPFD and TK magmas. This is not apparent from measured Sr and Ba content of bulk measurement. Furthermore, textural and chemical variations in EPD plagioclase indicate at least one distinct rejuvenation and mingling event (Fig. 11). The An content jumps from 30 to 35-40 mol% and simultaneously, Sr content increases, while Ba, La, Ce and Pb decrease (Fig. 11), suggesting influx and interaction with a more mafic magma. Some plagioclase crystals of the EPD contain large xenocrystic cores with chemistry similar to plagioclase of the TK and NPFD, and almost identical to those of the GRT unit of the TK (Fig. 13d). This would suggest that two reservoirs were active at the same time, because the ascending rhyolites must have percolated thorough the mush zone that formed the NPFD and TK. The abundance of small Mg-rich orthopyroxene crystals in the rhyolites of the EPD provides additional support for the interaction of the rhyolitic magma with the Nyukawa reservoir (Fig. 8d). Finally the time between the two eruptions is estimated to be 10 kyr (Yoshikawa *et al.*, 1996). This provides a maximum timescale for the formation of the crystal rims around the xenocrystic cores. It is debatable whether the percolation of the rhyolitic melt occurred after the eruption of the NPFD, or whether a rhyolitic reservoir had already formed at the time of the NPFD eruption. In the latter case, the eruption of the NPFD and associated decompression of the mush column could have led to the destabilisation of the CT-EPD reservoir and to the onset of rhyolitic eruptions. This would also imply that in mature systems, in which multiple reservoirs co-exist no additional input are required to trigger a sequence of large volcanic eruptions (Curry *et al.*, 2021).

Some magma must have remained in the crust after the eruption of the NPFD and CT-EPD. Magma cooling and crystallisation of younger zircon crystals also must have occurred after the volcanic activity. We can, therefore, expect to find zircon populations in the remaining plutonic rocks that are younger than the volcanic eruptions. Otherwise, we would need to imply that the magmatic system cooled immediately below solidus at the moment of eruption, which is not thermally feasible. The zircon crystallisation ages of the TK (i.e. 1.1-1.6 Ma; Ito et al. 2017; Farina et al. 2020, 2021) are slightly younger than the eruption age of the volcanic units (i.e. 1.75-1.76 Ma; Yoshikawa et al. 1996; Harayama 1998). This could mean that the TK magmas were emplaced after the eruption of the NPFD and CT-EPD. Alternatively, TK magmas could have already been present when the eruption occurred. A detailed geochronological study (e.g. U-Pb zircon geochronology) of the three volcanic units would clarify the relationship between the HA, NPFD and CT-EPD, and help to understand if the TK magmas were already present at the time of eruption. In the latter case, the basal units of the HA would need to be older than 1.76 Ma (i.e. eruption age of the NPFD), because the TK intruded at the base of the HA and is therefore younger.

Considering that the total erupted magma volume of the NPFD and CT-EPD of about 500 km^3 accumulated over a time period of approximately 500-600 kyr (i.e. using the range in zircon crystallisation ages recorded in the TK), we can assume a minimum magma flux of 0.8-1.0 x 10^{-3} km^3 yr^{-1}. If we consider a footprint for the TK magmatic system of 200-300 km^2 and a thermally matured crust, to accumulate such volume of eruptible magma in about 600 kyr requires rates of magma injection in the upper crust of the order of 1.0-1.5 x 10^{-3} km^3 yr^{-1} (Karakas et al., 2017). This implies that the erupted magma represents 50-80% of the total injected magma. These estimates are similar to those of the caldera-forming Minoan eruption in Santorini (Druitt *et al.*, 2012).

Our results show compelling evidence for a genetic link between the TK and some large volcanic eruptions, the products of which are distributed over a large portion of Japan. While the dacitic magma of the NPFD is similar to the TK granodiorite and was produced chiefly by magma fractionation, partial melting and assimilation of crustal lithologies were more important in the rhyolite generation of the CT-EPD. Moreover, plagioclase chemistry indicates that the dacite and rhyolite erupted from a vertically extended mush column. Pressure estimates and oxygen fugacities of the CT-EPD indicate that the rhyolitic melts were extracted from the lower mush column, that had experienced a higher degree of crustal assimilation. The TK crystallised and solidified after the eruption of the NPFD and CT-EPD, but TK magmas may have already been present at the time of eruption. Overall, the thermal maturation of the upper crust by repeated magma injection over hundreds of thousands of years led to two large eruptions in short succession and formation of the TK.

CONCLUSION

The Takidani pluton (TK) and products of two associated volcanic eruptions provide a window into upper crustal magmatism and the build-up phase to large explosive volcanic eruptions. Our results suggest that the magmatic system was growing progressively until it thermally matured sufficiently to feed two large volcanic eruptions in short succession (Fig. 15). Magma injection into the upper crust (<10 km) first led to accumulation and crystallisation of dacitic magma (Fig. 15). The emplacement and crystallisation of dacitic magmas, and thermal maturation of the system occurred contemporaneously with the Ueno magmatism over many hundreds of thousands to millions of years from ca. 2.7 Ma to ca. 1.1 Ma (i.e. zircon fission track and U-Pb ages; Harayama 1998; Kimura and Yoshida 1999; Ito et al. 2017; Farina et al. 2020, 2021). During the initial stages of volcanism, assimilation of crustal lithologies played a minor role in the chemical evolution of the dacitic magmas.

However, the progressive thermal maturation of the crust led to an increased contribution of assimilation of lower crustal lithologies that promoted the formation of the more reduced rhyolite (Fig. 9).

Plagioclase and amphibole dominated fractionation was largely responsible for generating the calc-alkaline dacitic compositions of the TK, Hotaka Andesite (i.e. caldera fill deposit, HA) and Nyukawa Pyroclastic Flow Deposit (i.e. caldera outflow deposit, NPFD). Plagioclase chemistry suggests that magma rejuvenation led to the reactivation of the shallow storage zone and the eruption of crystal-rich dacite (>400 km^3 DRE) at ca. 1.76 Ma (Fig. 15). Approximately 10 kyr later, more than 100 km^3 DRE of rhyolitic magma was erupted from the same magmatic system forming the Chayano Tuff and Ebisutoge Pyroclastic Deposits (CT-EPD; 1.75 Ma, Fig. 15). Xenocrystic cores in plagioclase of the Ebisutoge rhyolite provide evidence that the rhyolitic melts percolated and accumulated within the dacitic (Nyukawa-Takidani) mush zone prior to eruption. After the eruption of the NPFD and CT-EPD, dacitic magma continued to form and to be emplaced in the upper crust until about 1.1 Ma forming the TK (Fig. 15; Farina et al. 2020, 2021).

The TK was emplaced at depths similar to those for the pre-eruptive storage conditions of the NPFD, while the rhyolite of the CT and EPD were stored over a range of depths that correspond to the deepest portion of TK (i.e. ca. 10 km; Hartung et al. 2017). A reservoir of >100 km^3 of crystal-poor rhyolites (i.e. CT and EPD) could have developed prior to the eruption of the NPFD. Alternatively, the eruption of the NPFD could have promoted the rapid extraction and accumulation of the rhyolitic melts from the vertically connected mush column (Fig. 15).

If the pre-eruptive sequence of events we identified for the pluton and associated volcanic units is applicable to other active volcanic systems, large eruptions occur at a ‘thermal optimum’ and without significant variations of the conditions of magma

accumulation in the crust. Detecting the signs of an impending large eruption without any dramatic variation of the conditions of growth of the sub-volcanic magma reservoir would be an extremely complicated task.

DATA AVAILABILITY STATEMENT

The data underlying this article are available in the article's online supplementary material. The data underlying this article were collected as part of a doctoral study at the University of Geneva, Switzerland (Hartung, 2018), available at https://doi.org/10.13097/archive-ouverte/unige:112214. Major and trace element data of bulk rock analyses of the Takidani pluton collected in the Shiradashi-zawa valley (with exception of mafic enclaves and loose rock samples) are also available in Hartung et al. (2017) at https://doi.org/10.1093/petrology/egx033. Third-party geochemical data underlying this article can be obtained from Kimura and Nagahashi (2007) at https://doi.org/10.1016/j.jvolgeores.2007.02.004, and from Bando et al. (2003) at https://doi.org/10.1016/S0377-0273(02)00399-2.

ACKNOWLEDGMENTS

We would like to acknowledge and thank Jean-Marie Boccard for the preparation of numerous thin sections and Davide Roggero and Alexey Ulianov for their assistance with LA-ICP-MS analysis. We thank the editor and three anonymous reviewers who with their constructive feedback helped to significantly improve this manuscript. This project was funded by the Swiss National Science Foundation (200021_150204, 200020_172702). During the course of this study EH was also financially supported by the Japan Society for the Promotion of Science (GR17103) and SNSF Early Postdoc.Mobility (P2GEP2_184466). LC received additional funding from the European Research Council (ERC) under the

European Union's Horizon 2020 research and innovation program (grant agreement 677493-FEVER).

REFERENCES

Aigner-Torres, M., Blundy, J., Ulmer, P. & Pettke, T. (2007). Laser Ablation ICPMS study of trace element partitioning between plagioclase and basaltic melts: An experimental approach. *Contributions to Mineralogy and Petrology* **153**, 647–667.

Anderson, A. T., Swihart, G. H., Artioli, G. & Geiger, C. A. (1984). Segregation vesicles, gas filter-pressing, and igneous differentiation. *Journal of Geology* **92**, 55–72.

Andrews, B. J. (2014). Magmatic storage conditions, decompression rate, and incipient caldera collapse of the 1902 eruption of Santa Maria Volcano, Guatemala. *Journal of Volcanology and Geothermal Research* **282**, 103–114.

Annen, C., Blundy, J. D. & Sparks, R. S. J. (2006). The Genesis of Intermediate and Silicic Magmas in Deep Crustal Hot Zones. *Journal of Petrology* **47**, 505–539.

Bachl, C. A., Miller, C. F., Miller, J. S. & Faulds, J. E. (2001). Construction of a pluton: Evidence from an exposed cross section of the Searchlight pluton, Eldorado Mountains, Nevada. *Geological Society of America Bulletin* **113**, 1213–1228.

Bachmann, O. & Bergantz, G. (2004). On the Origin of Crystal-poor Rhyolites : Extracted from Batholithic Crystal Mushes. *Journal of Petrology* **45**, 1565–1582.

Bachmann, O. & Bergantz, G. (2008). The magma reservoirs that feed supereruptions. *Elements* **4**, 17.

Bachmann, O. & Bergantz, G. W. (2006). Gas percolation in upper-crustal silicic crystal mushes as a mechanism for upward heat advection and rejuvenation of near-solidus magma bodies. *Journal of Volcanology and Geothermal Research* **149**, 85–102.

Bachmann, O. & Huber, C. (2019). The Inner Workings of Crustal Distillation Columns; the Physical Mechanisms and Rates Controlling Phase Separation in Silicic Magma Reservoirs. *Journal of Petrology* **60**, 3–18.

Bando, M., Bignall, G., Sekine, K. & Tsuchiya, N. (2003). Petrography and uplift history of the

Quaternary Takidani Granodiorite : could it have hosted a supercritical (HDR) geothermal reservoir? *Journal of Volcanology and Geothermal Research* **120**, 215–234.

Barbarin, B. (2005). Mafic magmatic enclaves and mafic rocks associated with some granitoids of the central Sierra Nevada batholith, California: nature, origin, and relations with the hosts. *Lithos* **80**, 155–177.

Barker, S. J., Wilson, C. J. N., Morgan, D. J. & Rowland, J. V. (2016). Rapid priming, accumulation, and recharge of magma driving recent eruptions at a hyperactive caldera volcano. *Geology* **44**, 323–326.

Blatter, D. L., Sisson, T. W. & Hankins, W. Ben (2013). Crystallization of oxidized, moderately hydrous arc basalt at mid- to lower-crustal pressures: Implications for andesite genesis. *Contributions to Mineralogy and Petrology* **166**, 861–886.

Bowen, N. (1928). *The Evolution of Igneous Rocks*. Princeton: Princeton University Press.

Cashman, K. V., Sparks, R. S. J. & Blundy, J. D. (2017). Vertically extensive and unstable magmatic systems: A unified view of igneous processes. *Science* **355**.

Coleman, D. S., Gray, W. & Glazner, A. F. (2004). Rethinking the emplacement and evolution of zoned plutons: Geochronologic evidence for incremental assembly of the Tuolumne Intrusive Suite, California. *Geology* **32**, 433–436.

Costa, F., Scaillet, B. & Pichavant, M. (2004). Petrological and Experimental Constraints on the Pre-eruption Conditions of Holocene Dacite from Volcan San Pedro (36°S, Chilean Andes) and the Importance of Sulphur in Silicic Subduction-related Magmas. *Journal of Petrology* **45**, 855–881.

Curry, A., Caricchi, L. & Lipman, P. W. (2021). Magmatic evolution of zoned and unzoned ignimbrites: evidence for a complex crustal architecture feeding four rapid-sequence, caldera-forming eruptions in the San Juan Mountains, Colorado. *Journal of Petrology* **62**, egab006.

Davis, M., Koenders, M. A. & Petford, N. (2007). Vibro-agitation of chambered magma. *Journal of Volcanology and Geothermal Research* **167**, 24–36.

Deering, C. D. & Bachmann, O. (2010). Trace element indicators of crystal accumulation in silicic igneous rocks. *Earth and Planetary Science Letters* **297**, 324–331.

Deering, C. D., Keller, B., Schoene, B., Bachmann, O., Beane, R. & Ovtcharova, M. (2016). Zircon

record of the plutonic-volcanic connection and protracted rhyolite melt evolution. *Geology* **44**, 267–270.

Drake, M. J. & Weill, D. F. (1975). Partition of Sr, Ba, Ca, Y, Eu2+, Eu3+, and other REE between plagioclase feldspar and magmatic liquid: an experimental study. *Geochimica et Cosmochimica Acta* **39**, 689–712.

Druitt, T. H., Costa, F., Deloule, E., Dungan, M. & Scaillet, B. (2012). Decadal to monthly timescales of magma transfer and reservoir growth at a caldera volcano. *Nature* **482**, 77–80.

Ducea, M. N., Bergantz, G. W., Crowley, J. L. & Otamendi, J. (2017). Ultrafast magmatic buildup and diversification to produce continental crust during subduction. *Geology* **45**, 235–238.

Dufek, J. & Bachmann, O. (2010). Quantum magmatism: Magmatic compositional gaps generated by melt-crystal dynamics. *Geology* **38**, 687–690.

Dufek, J. & Bergantz, G. (2005). Lower Crustal Magma Genesis and Preservation : a Stochastic Framework for the Evaluation of Basalt–Crust Interaction. *Journal of Petrology* **46**, 2167–2195.

Farina, F., Hartung, E., Weber, G., Rubatto, D. & Caricchi, L. (2021). When volcanic eruptions and shallow-level granites are siblings: the case of the Takidani magmatic complex. *Goldschmidt2021• Virtual• 4-9 July*.

Farina, F., Rubatto, D., Hartung, E. & Caricchi, L. (2020). Time and tempo of melt segregation from a magma mush: evidence from the Takidani pluton (Japan). *EGU General Assembly Conference Abstracts*, 8115.

Fiedrich, A. M., Bachmann, O., Ulmer, P., Deering, C. D., Kunze, K. & Leuthold, J. (2017). Mineralogical, geochemical, and textural indicators of crystal accumulation in the Adamello Batholith (Northern Italy). *American Mineralogist* **102**, 2467–2483.

Floess, D., Caricchi, L., Simpson, G. & Wallis, S. R. (2019). Melt segregation and the architecture of magmatic reservoirs: insights from the Muroto sill (Japan). *Contributions to Mineralogy and Petrology* **174**, 1–15.

Gelman, S. E., Deering, C. D., Bachmann, O., Huber, C. & Gutiérrez, F. J. (2014). Identifying the crystal graveyards remaining after large silicic eruptions. *Earth and Planetary Science Letters* **403**, 299–306.

Ghiorso, M. S. & Evans, B. W. (2008). Thermodynamics of Rhombohedral Oxide Solid Solutions and a Revision of the FE-TI Two-Oxide Geothermometer and Oxygen-Barometer. *American Journal of Science* **308**, 957–1039.

Ghiorso, M. S. & Gualda, G. a. R. (2015). An H2O–CO2 mixed fluid saturation model compatible with rhyolite-MELTS. *Contributions to Mineralogy and Petrology* **169**, 1–30.

Ginibre, C., Wörner, G. & Kronz, A. (2002). Minor- and trace-element zoning in plagioclase: implications for magma chamber processes at Parinacota volcano, northern Chile. *Contributions to Mineralogy and Petrology* **143**, 300–315.

Glazner, A. F., Coleman, D. S. & Bartley, J. M. (2008). The tenuous connection between high-silica rhyolites and granodiorite plutons. *Geology* **36**, 183–186.

Global Volcanism Program (1995). Report on Yakedake (Japan). In: Wunderman, R. (ed.) *Bulletin of the Global Volcanism Network*. Smithsonian Institution.

Gualda, G. A. R. & Ghiorso, M. S. (2014). Phase-equilibrium geobarometers for silicic rocks based on rhyolite-MELTS. Part 1: Principles, procedures, and evaluation of the method. *Contributions to Mineralogy and Petrology* **168**, 1–17.

Gualda, G. A. R., Ghiorso, M. S., Lemons, R. V. & Carley, T. L. (2012a). Rhyolite-MELTS: a Modified Calibration of MELTS Optimized for Silica-rich, Fluid-bearing Magmatic Systems. *Journal of Petrology* **53**, 875–890.

Gualda, G. A. R., Gravley, D. M., Conner, M., Hollmann, B., Pamukcu, A. S., Bégué, F., Ghiorso, M. S. & Deering, C. D. (2018). Climbing the crustal ladder: Magma storage-depth evolution during a volcanic flare-up. *Nature Communications* **4**, eaap7567.

Gualda, G. A. R., Gravley, D. M., Deering, C. D. & Ghiorso, M. S. (2019). Magma extraction pressures and the architecture of volcanic plumbing systems. *Earth and Planetary Science Letters* **522**, 118–124.

Gualda, G. A. R., Pamukcu, A. S., Ghiorso, M. S., Anderson, A. T., Sutton, S. R. & Rivers, M. L. (2012b). Timescales of Quartz crystallization and the longevity of the Bishop Giant Magma body. *PLoS ONE* **7**, e37492.

Hammer, J. E. & Rutherford, M. J. (2002). An experimental study of the kinetics of decompression-

induced crystallization in silicic melt. *Journal of Geophysical Research: Solid Earth* **107**, ECV 8.

Harayama, S. (1990). *Geology of the Kamikochi district with geological sheet map at 1:50000. Geological Survey of Japan*.

Harayama, S. (1992). Geology Youngest exposed granitoid pluton on Earth : Cooling and rapid uplift of the Pliocene-Quaternary Takidani Granidiorite in the Japan Alps, central Japan. *Geology* **20**, 657–660.

Harayama, S. (1998). Chronology and tectonic setting of the Hotaka-Takidani volcano-plutonic complex, and uplifting history of the Hida Mountain Range. *Abs. 105th Am. Meeting Geol. Soc. Japan*.

Harayama, S. (1999). Multistage upheaval and tectonics in the Hida Mountain Range. *Monthly Earth* **21**, 603–607.

Harayama, S., Takeuchi, M., Nakano, S., Sato, T. & Takizawa, F. (1991). Geology of the Yarigatake district with geological sheet map at 1:50000. Geological Survey of Japan, 190.

Harayama, S., Wada, H. & Yamaguchi, Y. (2003). Trip A1 Quaternary and Pliocene granites in the Northern Japan Alps. *Hutton Symposium V, Field Guidebook*. Geological Survey of Japan, Interim-Report no.28, 3–21.

Hartung, E. (2018). Silicic magmatism in the upper crust and relationships to caldera-forming eruptions: insights from the Takidani magmatic system in Central Japan. Université de Genève.

Hartung, E., Caricchi, L., Floess, D., Wallis, S., Harayama, S., Kouzmanov, K. & Chiaradia, M. (2017). Evidence for residual melt extraction in the Takidani Pluton, Central Japan. *Journal of Petrology* **58**, 763–788.

Hartung, E., Weber, G. & Caricchi, L. (2019). The role of H2O on the extraction of melt from crystallising magmas. *Earth and Planetary Science Letters* **508**, 85–96.

Hildreth, W. (1981). Gradients in silicic magma chambers: Implications for lithospheric magmatism. *Journal of Geophysical Research: Solid Earth* **86**, 10153–10192.

Hildreth, W. (2004). Volcanological perspectives on Long Valley , Mammoth Mountain , and Mono Craters : several contiguous but discrete systems. *Journal of Volcanology and Geothermal Research* **136**, 169–198.

Holness, M. B. (2018). Melt segregation from silicic crystal mushes: a critical appraisal of possible mechanisms and their microstructural record. *Contributions to Mineralogy and Petrology* **173**, 1–17.

Housh, T. B. & Luhr, J. F. (1991). Plagioclase-melt equilibria in hydrous systems. *American Mineralogist* **76**, 477–492.

Huber, C., Bachmann, O. & Manga, M. (2010). Two Competing Effects of Volatiles on Heat Transfer in Crystal-rich Magmas: Thermal Insulation vs Defrosting. *Journal of Petrology* **51**, 847–867.

Ito, H., Spencer, C. J., Danišík, M. & Hoiland, C. W. (2017). Magmatic tempo of Earth's youngest exposed plutons as revealed by detrital zircon U-Pb geochronology. *Scientific reports* **7**, 1–6.

Jackson, M. D., Blundy, J. & Sparks, R. S. J. (2018). Chemical differentiation, cold storage and remobilization of magma in the Earth's crust. *Nature* **564**, 405–409.

Jackson, S. E. (2008a). Calibration Strategies for Elemental Analysis by LA-ICP-MS. In: Sylvester, P. J. (ed.) *Laser Ablation-ICP-Mass Spectrometry in the Earth Sciences: Current Practices and Outstanding Issues*. Mineralogical Association of Canada Short Course Series, 169–188.

Jackson, S. E. (2008b). LAMTRACE data reduction software for LA-ICP-MS. In: Sylvester, P. J. (ed.) *Laser Ablation-ICP-Mass Spectrometry in the Earth Sciences: Current Practices and Outstanding Issues*. Mineralogical Association of Canada Short Course Series, 305–307.

Jackson, S. E., Longerich, H. P., Dunning, G. R. & Fryer, B. J. (1992). The application of laser-ablation microprobe-inductively coupled plasma-mass spectrometry (LAM-ICP-MS) to in situ trace element determination in minerals. *Canadian Mineralogist* **30**, 1049–1064.

Jagoutz, O. (2014). Arc crustal differentiation mechanisms. *Earth and Planetary Science Letters* **396**, 267–277.

Jagoutz, O. E., Burg, J. P., Hussain, S., Dawood, H., Pettke, T., Iizuka, T. & Maruyama, S. (2009). Construction of the granitoid crust of an island arc part I: geochronological and geochemical constraints from the plutonic Kohistan (NW Pakistan). *Contributions to Mineralogy and Petrology* **158**, 739–755.

Johannes, W. & Holtz, F. (1996). *Petrogenesis and Experimental Petrology of Granitic Rocks*. Berlin, Heidelberg, New York: Springer-Verlag.

Karakas, O., Wotzlaw, J. F., Guillong, M., Ulmer, P., Brack, P., Economos, R., Bergantz, G. W., Sinigoi, S. & Bachmann, O. (2019). The pace of crustal-scale magma accretion and differentiation beneath silicic caldera volcanoes. *Geology* **47**, 719–723.

Kataoka, K., Nagahashi, Y. & Yoshikawa, S. (2001). An extremely large magnitude eruption close to the Plio-Pleistocene boundary: reconstruction of eruptive style and history of the Ebisutoge-Fukuda tephra, central Japan. *Journal of Volcanology and Geothermal Research* **107**, 47–69.

Kimura, J.-I. & Nagahashi, Y. (2007). Origin of a voluminous iron-enriched high-K rhyolite magma erupted in the North Japan Alps at 1.75 Ma: Evidence for upper crustal melting. *Journal of Volcanology and Geothermal Research* **167**, 81–99.

Kimura, J.-I. & Yoshida, T. (1999). Mantle diapir-induced arc volcanism: The Ueno Basalts, Nomugi-Toge and Hida volcanic suites, central Japan. *The Island Arc* **8**, 304–322.

Kimura, J. I., Manton, W. I., Sun, C. H., Iizumi, S., Yoshida, T. & Stern, R. J. (2002). Chemical diversity of the Ueno Basalts, central Japan: Identification of mantle and crustal contributions to arc basalts. *Journal of Petrology* **43**, 1923–1946.

King, G. E., Tsukamoto, S., Herman, F., Biswas, R. H., Sueoka, S. & Tagami, T. (2020). Electron spin resonance (ESR) thermochronometry of the Hida range of the Japanese Alps: validation and future potential. *Geochronology* **2**, 1–15.

Kohlstedt, D. L. & Holtzman, B. K. (2009). Shearing Melt Out of the Earth: An Experimentalist's Perspective on the Influence of Deformation on Melt Extraction. *Annual Review of Earth and Planetary Sciences* **37**, 561–593.

Leake, B. E. *et al.* (1997). Nomenclature of Amphiboles: Report of the Subcommitee on Amphiboles of the International Mineralogical Assocation Commission on New Minerals and Mineral Names. *Mineralogical Magazine* **61**, 295–310.

Lee, C.-T. A. & Morton, D. M. (2015). High silica granites: Terminal porosity and crystal settling in shallow magma chambers. *Earth and Planetary Science Letters* **409**, 23–31.

Lee, C.-T. A., Morton, D. M., Farner, M. J. & Moitra, P. (2015). Field and model constraints on silicic melt segregation by compaction/hindered settling: The role of water and its effect on latent heat release. *American Mineralogist* **100**, 1762–1777.

Lipman, P. W. (1984). The Roots of Ash Flow Calderas in Western North America: Windows Into the Tops of Granitic Batholiths. *Journal of Geophysical Research* **89**, 8801–8841.

Lipman, P. W. & Bachmann, O. (2015). Ignimbrites to batholiths: Integrating perspectives from geological, geophysical, and geochronological data. *Geosphere* **11**, 705–743.

Longerich, H. P., Gunther, D. & Jackson, S. E. (1996). Elemental fractionation in laser ablation inductively coupled plasma mass spectrometry. *Fresenius Journal of Analytical Chemistry* **355**, 538–542.

Lowery Claiborne, L., Miller, C. F., Walker, B. A., Wooden, J. L., Mazdab, F. K. & Bea, F. (2006). Tracking magmatic processes through Zr/Hf ratios in rocks and Hf and Ti zoning in zircons: An example from the Spirit Mountain batholith, Nevada. *Mineralogical Magazine* **70**, 517–543.

Marsh, B. (2004). A magmatic mush column rosetta stone: The McMurdo Dry Valleys of Antarctica. *Eos, Transactions American Geophysical Union* **85**, 497.

Marsh, B. D. (1981). On the crystallinity, probability of occurrence, and rheology of lava and magma. *Contributions to Mineralogy and Petrology* **78**, 85–98.

Martel, C., Pichavant, M., Holtz, F., Scaillet, B., Bourdier, J.-L. & Traineau, H. (1999). Effects of fO2 and H2O on andesite phase relations between 2 and 4 kbar. *Journal of Geophysical Research: Solid Earth* **104**, 29,453-29,470.

McDonough, W. F. & Sun, S.-S. (1995). The composition of the Earth. *Chemical Geology* 223–253.

McKenzie, D. (1984). The Generation and Compaction of Partially Molten Rock. *Journal of Petrology* **25**, 713–765.

Miller, C. F., Watson, E. B. & Harrison, T. M. (1988). Perspectives on the source, segregation and transport of granitoid magmas. *Earth and Environmental Science Transactions of the Royal Society of Edinburgh* **79**, 135–156.

Müntener, O., Kelemen, P. B. & Grove, T. L. (2001). The role of H2O during crystallization of primitive arc magmas under uppermost mantle conditions and genesis of igneous pyroxenites: an experimental study. *Contributions to Mineralogy and Petrology* **141**, 643–658.

Müntener, O. & Ulmer, P. (2018). Arc crust formation and differentiation constrained by experimental petrology. *American Journal of Science* **318**, 64–89.

Nagahashi, Y. (1995). Plio-Pleistocene volcaniclastic formation in the Takayama Basin, Gifu prefecture - Stratigraphy and Petrography -. *Earth Science (Chikyu Kagaku)* **2**, 109–124.

Nagahashi, Y., Kosaka, T. & Hibi, N. (1996). Correlation of the late Pliocene large-scale pyroclastic flow deposits, Gifu and Nagano prefectures, central Japan - case study of the Nyukawa Pyroclastic Flow Deposit, Ebisutoge Pyroclastic Deposits and their correlative deposits. *Earth Science (Chikyu Kagaku)* **50**, 29–42.

Nagahashi, Y., Satoguchi, Y. & Yoshikawa, S. (2000). Correlation and stratigraphic eruption age of the pyroclastic flow deposits and wide spread volcanic ashes intercalated in the Pliocene-Pleistocene strata, central Japan. *The Journal of the Geological Society of Japan* **106**, 51–69.

Nandedkar, R. H., Ulmer, P. & Müntener, O. (2014). Fractional crystallization of primitive, hydrous arc magmas: an experimental study at 0.7 GPa. *Contributions to Mineralogy and Petrology* **167**, 1015.

Oikawa, T. (2003). The Spatial and Temporal Relationship between Uplifting and Magmatism in the Hida Mountain Range, Central Japan. *The Quaternary Research* **42**, 141–156.

Paulatto, M., Moorkamp, M., Hautmann, S., Hooft, E., Morgan, J. V. & Sparks, R. S. J. (2019). Vertically Extensive Magma Reservoir Revealed From Joint Inversion and Quantitative Interpretation of Seismic and Gravity Data. *Journal of Geophysical Research: Solid Earth* **124**, 11170–11191.

Petford, N., Cruden, A. R., McCaffrey, K. J. & Vigneresse, J. L. (2000). Granite magma formation, transport and emplacement in the Earth's crust. *Nature* **408**, 669–73.

Petford, N., Koenders, M. A. & Clemens, J. D. (2020). Igneous differentiation by deformation. *Contributions to Mineralogy and Petrology* **175**, 1–21.

Pistone, M. *et al.* (2015). Gas-driven filter pressing in magmas: Insights into in-situ melt segregation from crystal mushes. *Geology* **43**, 699–702.

Rutherford, M. J. & Devine, J. D. (1996). Preeruption Pressure-Temperature conditions and volatiles in the 1991 dacitic magma of Mount Pinatubo. *Fire and mud: eruptions and lahars of Mount Pinatubo, Philippines*. Seattle: PHIVOLCS and University of Washington, 751–766.

Rutter, E. H. & Neumann, D. H. K. (1995). Experimental deformation of partially molten Westerly

granite under fluid-absent conditions, with implications for the extraction of granitic magmas. *Journal of Geophysical Research* **100**, 15697.

Sano, Y., Tsutsumi, Y., Terada, K. & Kaneoka, I. (2002). Ion microprobe U-Pb dating of Quaternary zircon: implication for magma cooling and residence time. *Journal of Volcanology and Geothermal Research* **117**, 285–296.

Schaen, A. J., Cottle, J. M., Singer, B. S., Brenhin Keller, C., Garibaldi, N. & Schoene, B. (2017). Complementary crystal accumulation and rhyolite melt segregation in a late Miocene Andean pluton. *Geology* **45**, 835–838.

Sisson, T. W. & Bacon, C. R. (1999). Gas-driven filter pressing in magmas. *Geology* **27**, 613–616.

Sisson, T. W., Ratajeski, A. K., Hankins, A. W. B. & Glazner, A. F. (2005). Voluminous granitic magmas from common basaltic sources. *Contributions to Mineralogy and Petrology* **148**, 635–661.

Sparks, R. S. J., Annen, C., Blundy, J. D., Cashman, K. V, Rust, A. C. & Jackson, M. D. (2019). Formation and dynamics of magma reservoirs. *Philosophical Transactions of the Royal Society A* **377**, 20180019.

Sueoka, S., Tsutsumi, H. & Tagami, T. (2016). New approach to resolve the amount of Quaternary uplift and associated denudation of the mountain ranges in the Japanese Islands. *Geoscience Frontiers* **7**, 197–210.

Turnbull, R., Weaver, S., Tulloch, A., Cole, J., Handler, M. & Ireland, T. (2010). Field and geochemical constraints on mafic-felsic interactions, and processes in high-level arc magma chambers: An example from the Halfmoon Pluton, New Zealand. *Journal of Petrology* **51**, 1477–1505.

Ulmer, P., Kaegi, R. & Müntener, O. (2018). Experimentally derived intermediate to silica-rich arc magmas by fractional and equilibrium crystallization at 1·0 GPa: An evaluation of phase relationships, compositions, liquid lines of descent and oxygen fugacity. *Journal of Petrology* **59**, 11–58.

Vigneresse, J. L., Barbey, P. & Cuney, M. (1996). Rheological Transitions During Partial Melting and Crystallization with Application to Felsic Magma Segregation and Transfer. *Journal of*

Petrology **37**, 1579–1600.

Whalen, J. B. & Chappell, B. W. (1988). Opaque mineralogy and mafic mineral chemistry of I-and S-type granites of the Lachlan fold belt, Southeast Australia. *American Mineralogist* **73**, 281–296.

Wilke, M. & Behrens, H. (1999). The dependence of the partitioning of iron and europium between plagioclase and hydrous tonalitic melt on oxygen fugacity. *Contributions to Mineralogy and Petrology* **137**, 102–114.

Wyborn, D., Chappell, B. W. & Johnston, R. M. (1974). Three S-Type Volcanic Suites From the Lachlan Fold Belt, Southeast Australia. *Journal of Geophysical Research* **86**, 10335–10348.

Yamada, R. (1999). Cooling history analysis of granitic rock in the Northern Alps, central Japan. *The Earth Monthly* **21**, 803-810 (in Japanese).

Yoshikawa, S., Satoguchi, Y. & Nagahashi, Y. (1996). A widespread volcanic ash bed in the horizon close to the Pliocene-Pleistocene boundary : Fukuda-Tsujimatagawa-Kd38 volcanic ash bed occuring in central Japan. *Journal of Geological Society of Japan* **102**, 258–270.

Table 1: Summary of modal abundances of the Takidani pluton from Bando et al. (2003) and Hartung et al. (2017)

	mGT		pGT		GDT		GRT		fGT1	
Quartz	27.5	± 2.5	32.8	± 2.8	27.8	± 3.0	29.2	± 1.9	31.6	± 4.8
Alkali feldspar	14.9	± 3.4	22.5	± 5.3	15.1	± 3.7	22.0	± 4.3	23.4	± 3.8
Plagioclase	46.5	± 4.0	34.9	± 4.6	43.7	± 3.8	38.8	± 2.9	39.7	± 6.8
Biotite	6.8	± 1.5	6.5	± 1.2	7.2	± 1.2	5.3	± 1.0	4.1	± 1.2
Hornblende	3.5	± 1.9	2.6	± 2.3	5.3	± 2.4	3.7	± 1.4	0.3	± 0.5
Fe-Ti oxides	0.82	*	0.30-0.63	*	0.51-0.74	*	0.8	± 0.4	0.5	± 0.4
Apatite	0.27	*	0.17-0.29	*	0.24-0.28	*	tr		tr	
Titanite	0.17	*	0.12-0.36	*	0.13-0.25	*	tr		tr	
Epidote	0.02	*	0.12-0.26	*	0.12-0.27	*	na		na	
Zircon	0.02	*	0.01-0.02	*	0.02	*	na		na	
Kaolinite	0.12	*	0.00-0.02	*	0.00	*	na		na	
Others	0.12	*	0.45-0.86	*	0.56-0.96	*	na		na	

*QEMSCAN data from *Hartung et al. (2017)*

Table 2: Mineral fractions of the Nyukawa Pyroxlastic Flow Deposit (NPFD) and Chayano Tuff (CT) and Ebisutoge Pyroclastic Deposit (EPD) from Nagahashi (1995) and Nagahashi et al. (2000)

	NPFD	CT Unit I	CT Unit II	EPD Unit A	EPD Unit B1	EPD Unit B2	EPD Unit C	EPD Unit D
Glass	2-95	96	98	93-99	98-99	98	86-99	98-99
Plagioclase	3-90	3	1-2	<6	1-2	1-2	<9	<1
Quartz	tr	1	tr	tr	tr	tr	<4	tr
Heavy minerals	1-8	tr	tr	tr	tr	tr	tr	tr
Heavy mineral fraction:								
Biotite	0	tr	tr	tr	<1	<1	tr	tr
Hornblende	0	20-24	1-20	0	<6	2-5	<3	2
Orthopyroxene	26-57	1	<14	3-20	<24	1-13	4-21	<21
Clinopyroxene	6-22	tr	tr	tr	<1	tr	<2	tr
Zircon	1-2	1-2	<2	tr	1-2	2-3	<2	<1
Opaques	21-66	73-76	77-84	78-97	72-92	81-90	76-91	74-97

FIGURE CAPTION

Figure 1

(a) Location map of the Takidani Pluton (TK) and associated volcanic deposits in Central Japan. (b) Takidani-Hotaka Andesite plutonic-volcanic complex including sample locations and lithological units of the TK. (c) Cross-section through the plutonic-volcanic complex from NW to SE (red line, Fig. 1b) illustrating the uplift and eastward tilting of the caldera floor (i.e. Hotaka Andesite, HA) and underlying magmatic reservoir (i.e. TK). Modified from (Harayama, 1990). Coordinate Reference System JGD2011.

Figure 2

(a) Yake-dake and Norikura volcanoes of the active volcanic Norikura volcanic chain. View from Nishiho-track toward the South. (b) Okuhotaka-dake and Hotaka Andesite (HA). View from Nishihotaka-dake toward the North. (c) Approximate magmatic contact of the Takidani Pluton (TK) and HA, and Cretaceous Kasagatake Rhyolite deposits. View from Nishiho-track across Nishiho-zawa toward the West. (d) Break-up of a mafic unit by the intrusion of granodioritic magma seen in a river boulder in the lower Shiradashi-zawa (e) Cross-cutting relationship of aplitic dikes with a rounded enclave embedded in TK granodiorite (f) Accumulation of felsic minerals in TK granodiorite observed in a river boulder in the lower Shiradashi-zawa valley. Diffuse margins and wavy texture indicate localised segregation and accumulation of residual melt.

Figure 3

Lithological units of the Takidani pluton from top to bottom: (a) marginal medium-grained porphyritic granodiorite (mGT) along the roof-contact with the Hotaka Andesite, (b) porphyritic fine-grained granite (fGT2) observed as isolated unit at the top of Nishiho-zawa

valley, (c) fine-grained porphyritic granodiorite and granite (pGT), interpreted as segregated melt from the underlying unit (Hartung *et al.*, 2017), (d) medium-grained equigranular hornblende granodiorite (GDT), (e) fine-to-medium-grained granodiorite (GRT), and (f) fine-to-medium grained biotite granite (fGT1) along the western tectonic contact.

Figure 4

(a) Stratigraphic column of pyroclastic flow deposits in the Takayama area after Nagahashi et al. (2000). (b) Exposure of the Nyukawa Pyroclastic Flow Deposit (NPFD) south of location 1 (Fig. 1a). (c) Thin section of dacitic welded tuff of the NPFD at location 2 (Fig. 1a). (d) Thin section of the welded ignimbrite of the Ebisutoge Pyroclastic Deposit (EPD; Unit D) displaying fiamme. (e) Exposure of the Chayano Tuff (CT) and EPD at location 1 (Fig. 1a).

Figure 5

Total alkalis versus silica diagram (i.e. normalised data) of published and new whole-rock and glass data of the Takidani pluton (TK; including mafic enclaves and aplitic dikes; purple), the Chayano Tuff and Ebisutoge Pyroclatic Deposit (CT-EPD; yellow), the Nyukawa Pyroclastic Flow Deposit (NPFD; blue) and the Hotaka Andesite (HA; black). HA2017 samples are published in Hartung et al. (2017). BD2003 samples are published in Bando et al. (2003). KN2007 samples are published in Kimura and Nagahashi (2007). Analytical uncertainties are smaller than the symbol size.

Figure 6

Major and trace element compositions are plotted against SiO_2 content (i.e. normalised data): (a-g) Al_2O_3, TiO_2, Fe_2O_3, MgO, MnO, CaO and Na_2O contents generally decrease with

increasing silica content in plutonic and volcanic rocks. CT-EPD samples have higher Al_2O_3 and MnO contents and lower TiO_2, MgO, CaO and Na_2O contents compared to plutonic counterparts. NPFD and CT-EPD samples overall display lower Na_2O contents of about 1 wt.% compared to plutonic rocks; (h) K_2O content is consistent in the plutonic and volcanic rocks and gradually increases with increasing silica content. (i-n) Mafic enclaves display a wide range in Rb and Sr concentrations from ca. 60 to 230 ppm and 200 to 550 ppm, respectively, while Rb and Sr concentrations of the pluton and volcanic units gradually increase and decrease with increasing silica content, respectively. (k) Ba content increases with increasing SiO_2 content, with the exception of aplitic dikes, which display a sharp decrease in Ba content. (l) Zr concentrations vary widely and are relatively enriched in NPFD and CT-EPD samples. (m,n) Rhyolite samples plot in a distinct group within Ba-Sr and Zr-Nb variation diagrams. Analytical uncertainties are smaller than the symbol size.

Figure 7

Spider diagrams of the (a) Takidani pluton (TK) and (b) volcanic units (i.e. HA, NPFD, CT-EPD). All units display comparable trace element patterns. The TK granite and CT-EPD rhyolite have more pronounced negative Sr and Eu anomalies compared to granodiorite and dacite samples. (c) The TK granodiorite and NPFD dacite have overlapping Rare Earh Elements (REE) patterns. HA displays a slight positive Eu anomaly. (d) REE patterns are comparable for the CT-EPD rhyolite and TK granite, but REE concentrations are generally higher in the rhyolite samples (i.e. bulk, pumice and glass). Values are normalised to Chondrite concentration of McDonough and Sun (1995). HA – Hotaka Andesite; NPFD – Nyukawa Pyroclastic Flow Deposit; CT-EPD – Chayano Tuff and Ebisutoge Pyroclatic Deposit.

Figure 8

Electron back-scattered images of NPFD and EPD thin sections with mineral spot analyses. (a) Magnetite (mg) and ilmenite (il) pair in the NPFD. (b) Albite (ab) and Fe-rich amphibole (am) inclusions in an orthopyroxene (opx) glomerocryst of the EPD. (c) Mg-rich orthopyroxene and plagioclase (pl) phenocrysts of the NPFD. (d) Fe-rich orthopyroxene phenocrysts and smaller Mg-rich orthopyroxene crystals of the EPD. gl – Glass; zr – zircon; Mg# –Magnesium number.

Figure 9

Oxygen fugacity and temperature estimates from magnetite-ilmenite equilibria using Ghiorso and Evans (2008). The oxygen fugacity of the NPFD ranges between NNO-0.1 to NNO+0.7. Temperature estimates for the NPFD vary between ca. 800°C to 920°C illustrating a large temperature gradient in magma reservoir. Oxygen fugacity and temperature values for the CT and EPD are obtained from Figure 10 of Kimura and Nagahashi (2007). One sample of the CT rhyolite records a high average temperature of 920°C and oxygen fugacity of NNO+0.7 similar to NPFD. Iron oxides reveal more reduced conditions for the EPD rhyolites with oxygen fugacities ranging from NNO-1.0 to NNO-2.1. Temperature estimates of the EPD are between 720°C to 790°C. All values are calculated and plotted for a pressure of 300 MPa. All values of the NPFD represent average values for each magnetite-ilmenite pair analysed in two samples. Estimates of the CT and EPD are mean values for each sample. NPFD – Nyukawa Pyroclastic Flow Deposit; CT – Chayano Tuff; EPD – Ebisutoge Pyroclastic Deposit.

Figure 10

Density plot of Mg numbers of pyroxene and amphibole analyses. Orthopyroxene (opx) of the NPFD (Nyukawa Pyroclastic Flow Deposit) and amphibole (am) of the TK (Takidani pluton) have the same average Mg numbers of about 0.6. Magnesium numbers of orthopyroxene and amphibole of the EPD (Ebisutoge Pyroclastic Deposit) range between ca. 0.3 and 0.4, with the exception of a few Mg-rich orthopyroxene (Fig. 8d). Pyroxene analyses of Kimura and Nagahashi (2007) are plotted for comparison in grey as vertical lines for single quantitative analyses and as kernel density estimation (including clinopyroxene; cpx).

Figure 11

Back-scattered electron images and chemical profiles of selected plagioclase crystals from the EPD (i.e. sample EH63.3 and EH65b), NPFD (i.e. sample EH61) and TK (i.e. sample EH70). The composition of the xenocrystic cores in EPD plagioclase corresponds to plagioclase profiles of NPFD and TK. Plagioclase of the EPD show distinctively higher Eu concentrations as the xenocrystic core. Anorthite (An) and FeO content were obtained along transects (black line) using an electron microprobe. Trace element concentration were obtained from 50 to 100 µm spot analysis (white circles) using LA-ICP-MS. EPD – Ebisutoge Pyroclastic Deposit; NPFD – Nyukawa Pyroclastic Flow Deposit; TK – Takidani Pluton.

Figure 12

Compositional variability of 18 plagioclase phenocrysts from the Takidani pluton (TK), Nyukawa Pyroclatic Flow Deposit (NPFD) and Ebisutoge Pyroclatic Deposit (EPD). (a) FeO vs. An content. (b) Sr variations in plagioclase of plutonic and volcanic rocks. EPD plagioclase displays a distinct Sr-An trend with higher Sr contents. Xenocrystic cores in EPD

plagioclase plot together with the NPFD and TK analyses. TK plagioclase cores show a diffuse Sr distribution at high An contents. (c) Concentrations of Eu in EPD plagioclase grains are twice as high as in plagioclase grains of the NPFD, the TK and EPD xenocrystic cores. (d) EPD plagioclase grains are enriched in Ba while rim compositions of the TK are depleted in Ba.

Figure 13

Rare Earth Elements (REE) analyses in plagioclase phenocrysts. (a) Spot analyses along mineral transects of plagioclase from four lithological units of the TK. Composition of the main growth zone (i.e. An_{32-57}) are illustrated in shades of purple. Rim compositions ($<An_{30}$) are shown in grey. (b) Plagioclase compositions of the NPFD overlap with analyses of the TK granodiorite. (c) Xenocrystic cores in EPD plagioclase are enriched in REE compared to EPD plagioclase main growth and rim compositions. (d) Xenocrystic cores in EPD plagioclase crystals overlap in compositions with plagioclase analyses of the GRT unit of the TK. All analyses present individual analysis. TK – Takidani Pluton; NPFD – Nyukawa Pyroclastic Flow Deposit; EPD – Ebisutoge Pyroclastic Deposit; GRT – fine-to-medium-grained granodiorite; GDT – medium-grained equigranular hornblende granodiorite; pGT – fine-grained porphyritic granodiorite and granite; mGT – marginal medium-grained porphyritic granodiorite.

Figure 14

Storage and eruption pressures estimated from glass and pumice composition using rhyolite-MELTS (Gualda and Ghiorso, 2014; Ghiorso and Gualda, 2015; Gualda *et al.*, 2019). (a) Distribution of pressure estimates of rhyolites from Units B to D of the EPD. The average extraction pressure (i.e. 273 MPa) of the three Units is about 80 MPa lower than the

estimated storage pressure of the same units (i.e. 195 MPa). (b) Extraction pressures derived from pumice analyses of the CT and EPD (Kimura and Nagahashi, 2007). Rhyolite extraction pressure increases for higher stratigraphic levels from about 180 MPa (i.e. CT) to 310 MPa (i.e. Unit C, EPD). The youngest and most voluminous Unit D of the EPD shows the largest spread in pressures from about 210 MPa to 350 MPa. Estimated and maximum errors of the Q1F are about 25 MPa and 95 MPa, respectively (Gualda and Ghiorso, 2014). EPD – Ebisutoge Pyroclastic Deposit; CT – Chayano Tuff.

Figure 15

Silicic volcanism in the Hida Mountains, Central Japan, and formation of the Takidani pluton (TK). (1) Thermal maturation of the upper crust by repeated magma injection and accumulation of dacitic magma led to the formation of a crystal mush and magma reservoir below Mount Ohuhotaka-dake (ca. 2.7 to 1.76 Ma). (2) New magma injection leads to the reactivation and eruption of the crystal-rich Nyukawa Pyroclastic Flow Deposit (NPFD, caldera outflow) and Hotaka Andesite (HA, caldera fill) at ca. 1.76 Ma. (3) Rhyolitic melts are extracted from the deeper parts of a vertically extended mush column, percolate and accumulate within the NPFD mush zone prior to eruption. A sequence of rhyolitic eruptions occurs at ca. 1.75 Ma forming the Chayano Tuff and Ebisutoge Pyroclastic Deposit (CT-EPD). (4) Dacitic magmas continue to be emplaced in the shallow crust after the eruption of the NPFD and CT-EPD until ca. 1.1 Ma forming the Takidani pluton (TK). Rapid uplift and denudation of the Hida Mountains leads to the exposure of the HA and TK. The magmatic system remains active at present with Yake-dake volcano located at the southern margin of the Takidani-Hotaka plutonic-volcanic complex.

Figure 1.

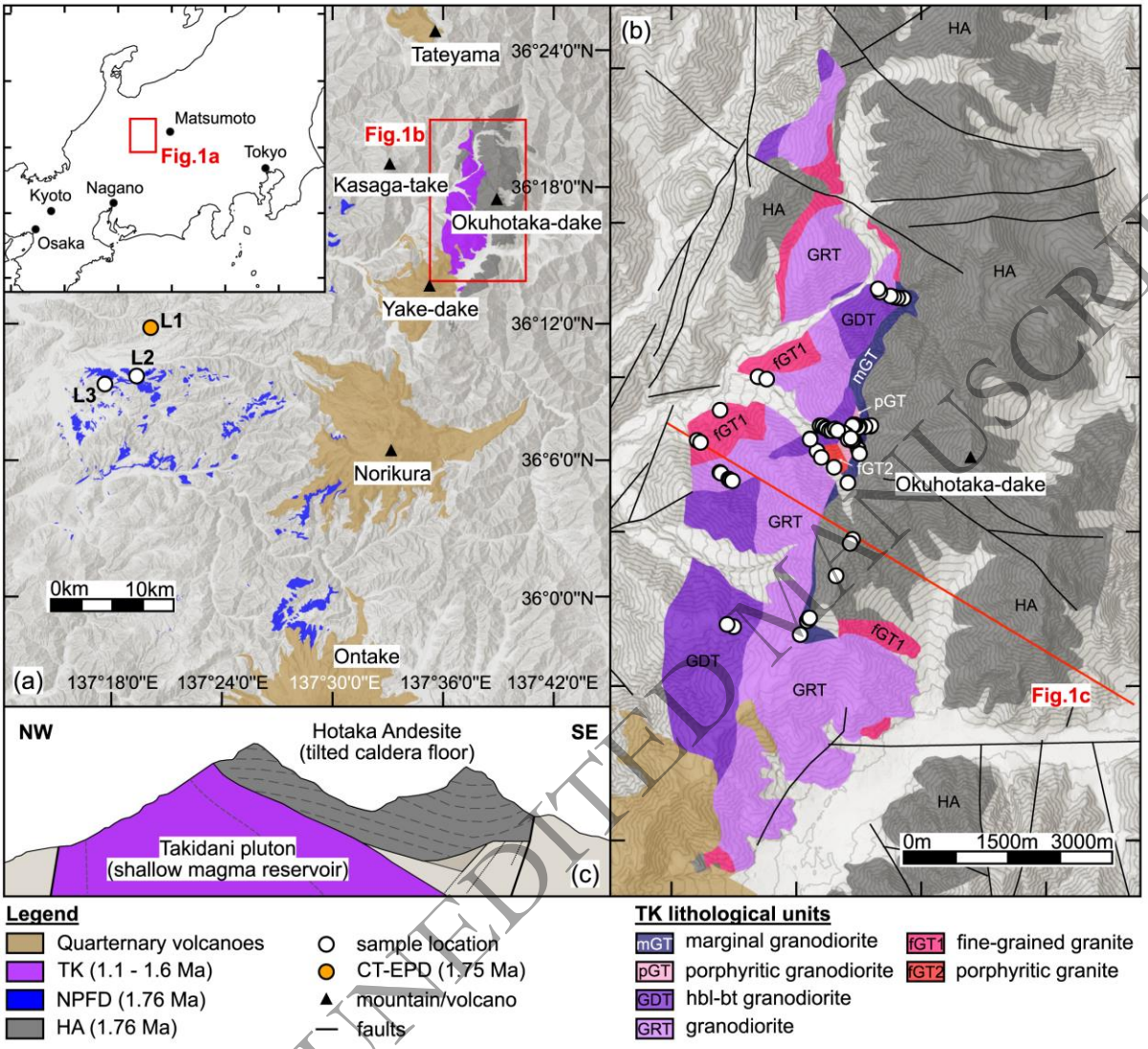

Figure 2.

Figure 3.

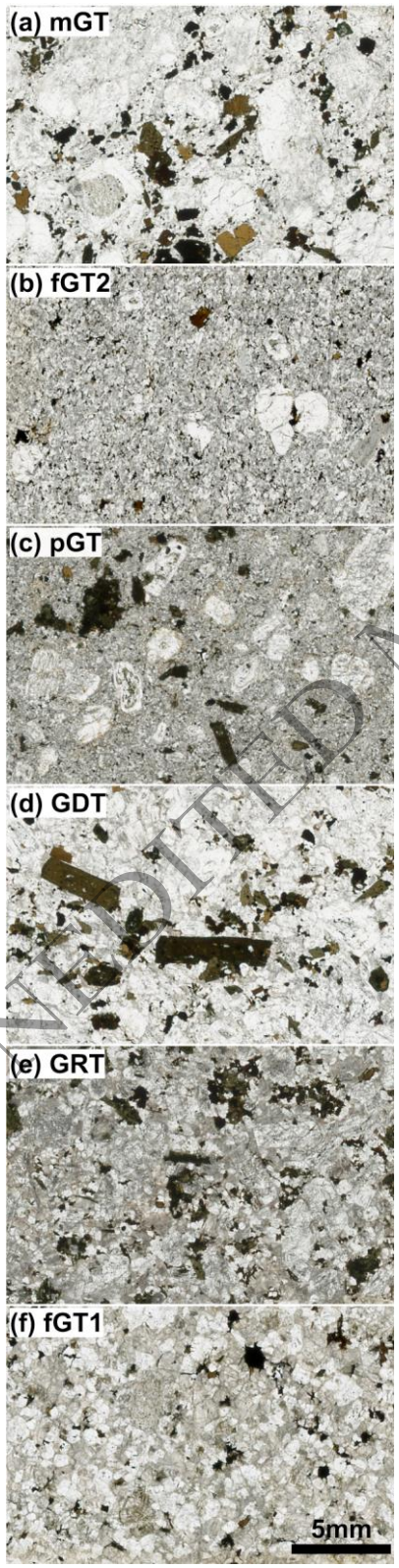

Figure 4.

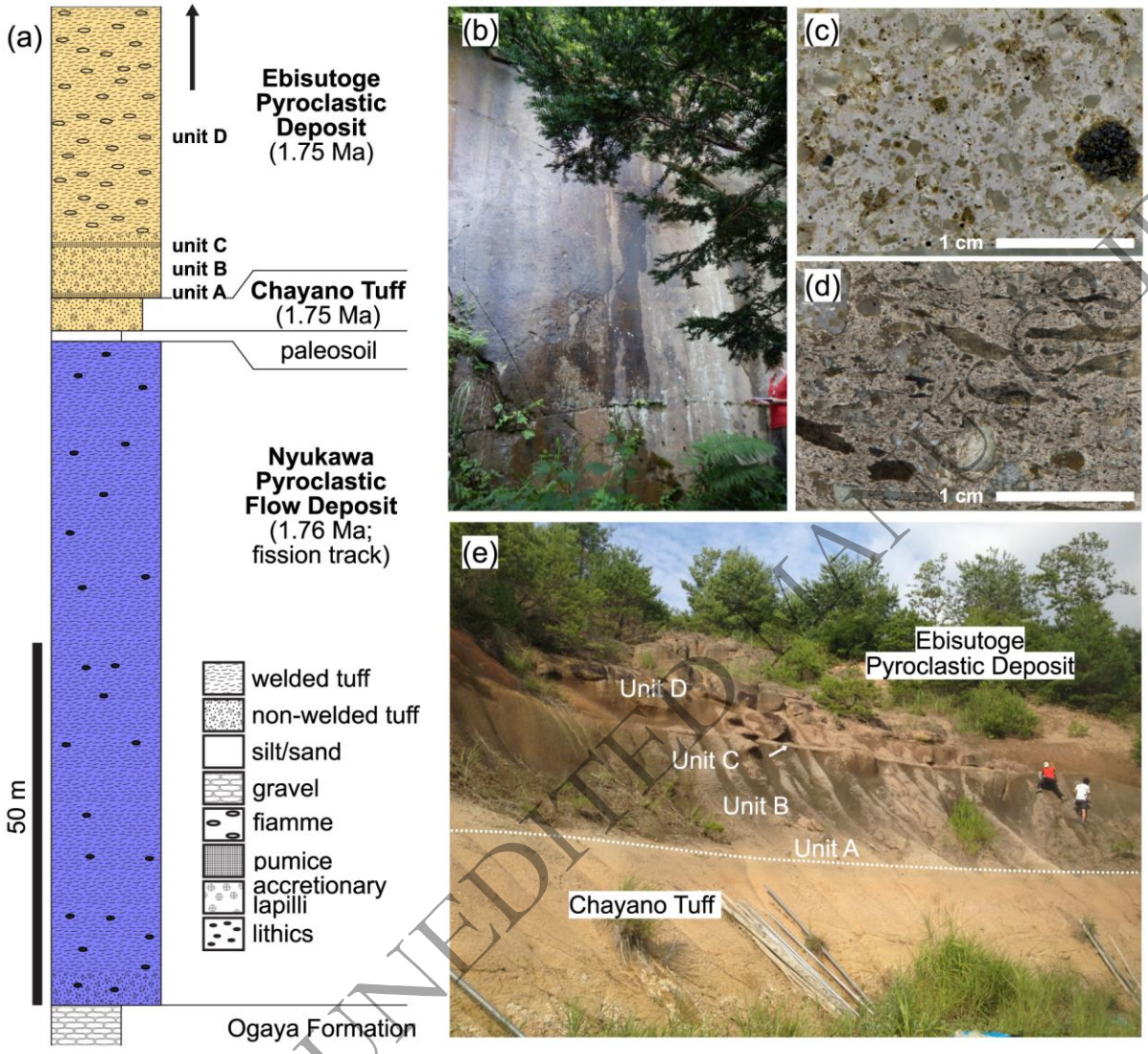

Figure 5.

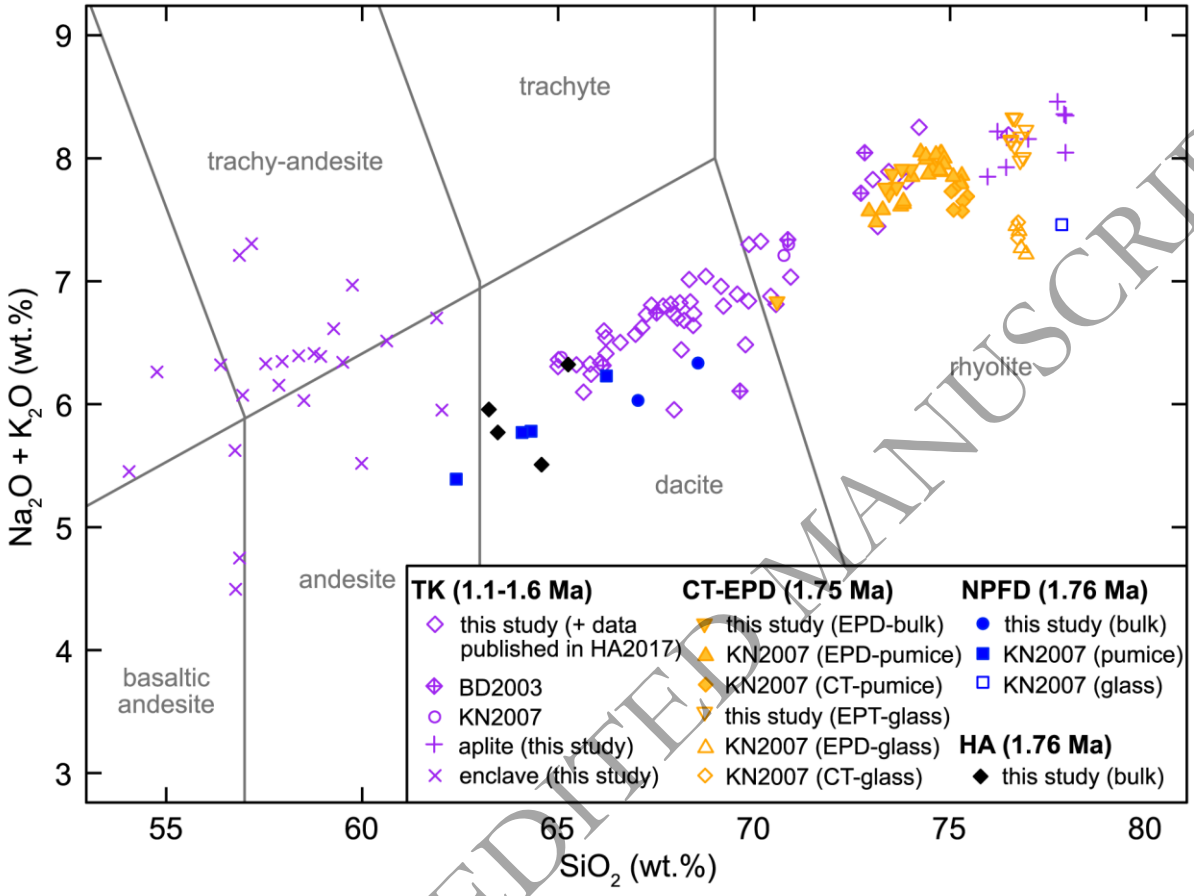

Figure 6.

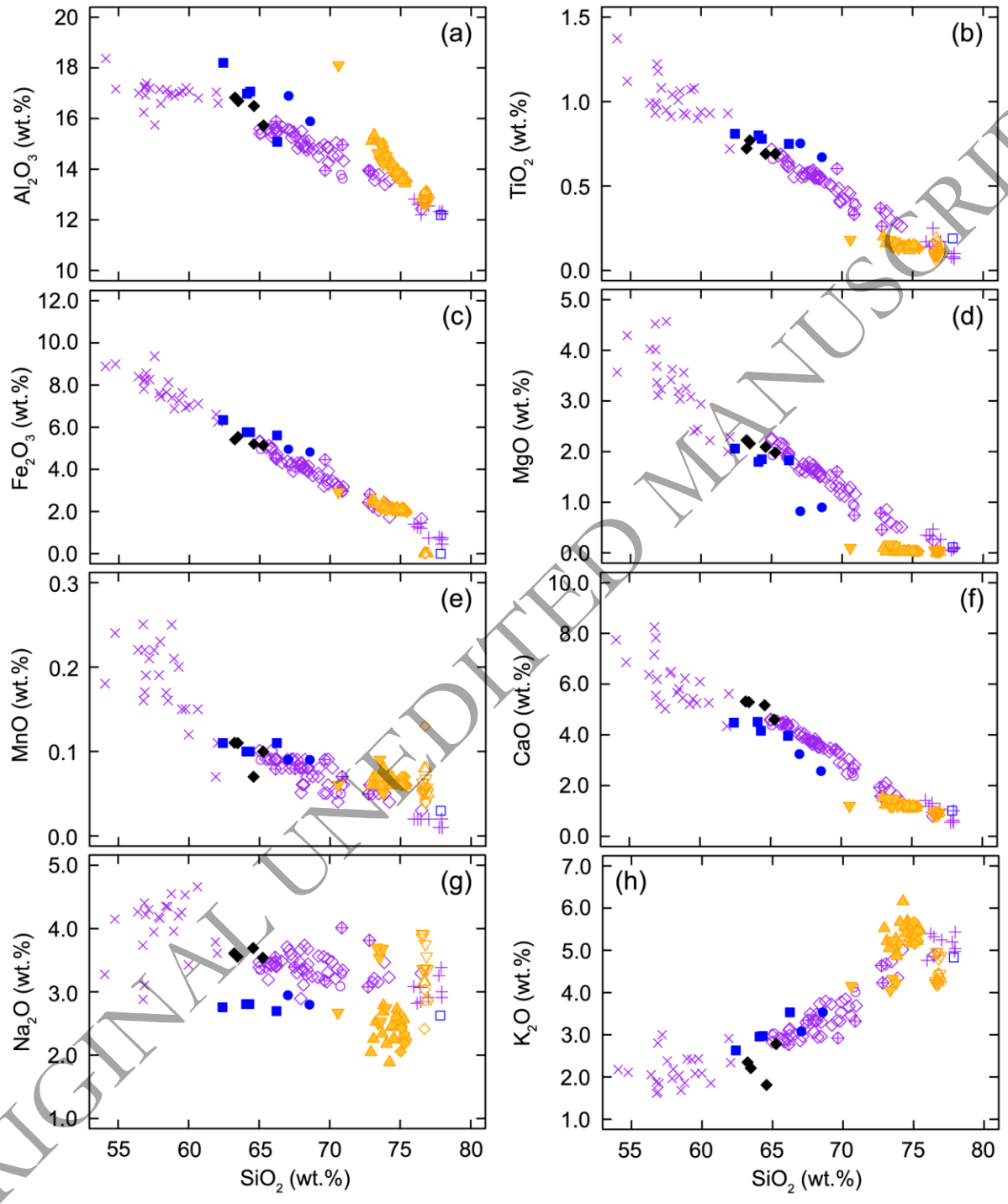

Figure 6 continued.

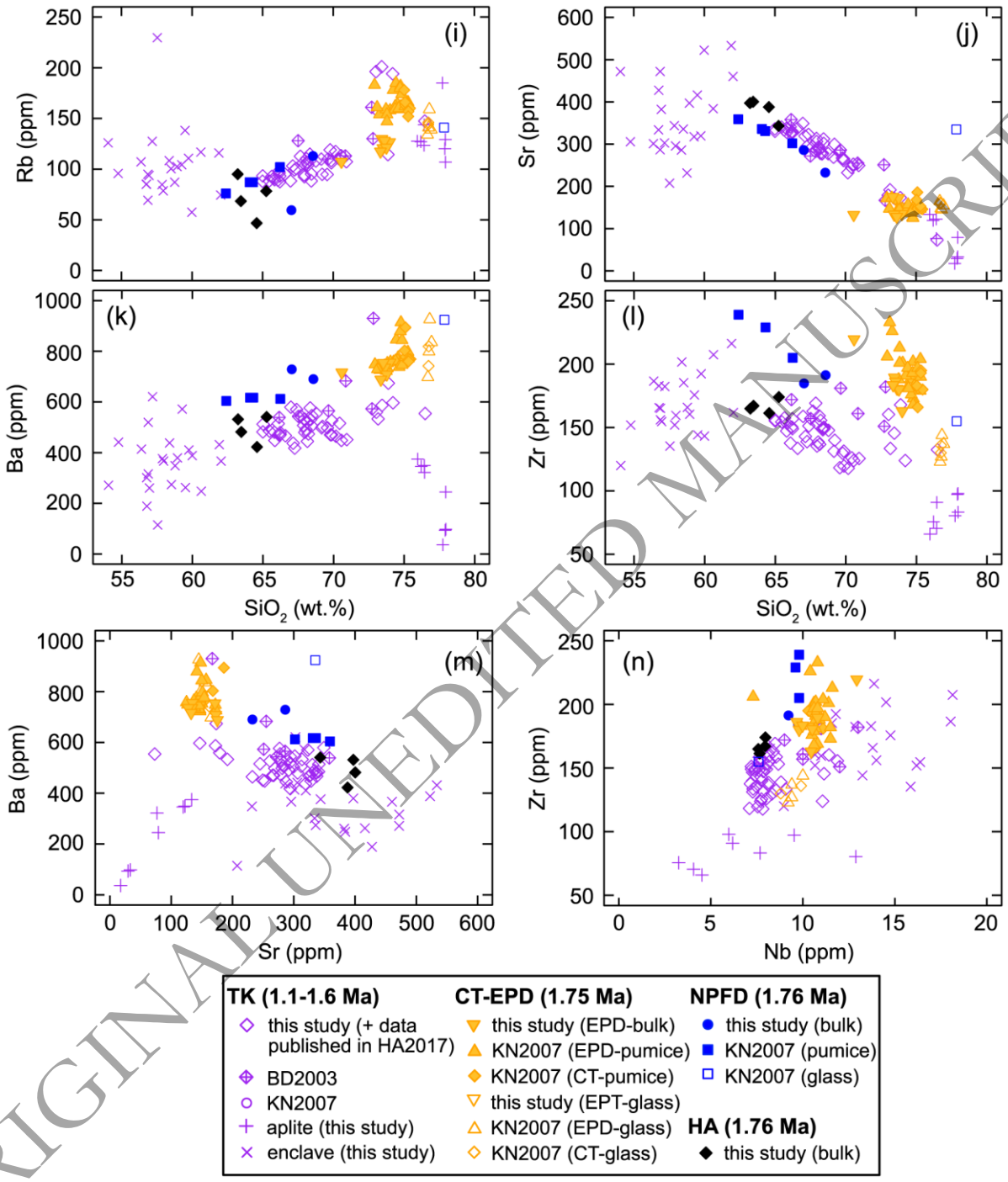

Figure 7.

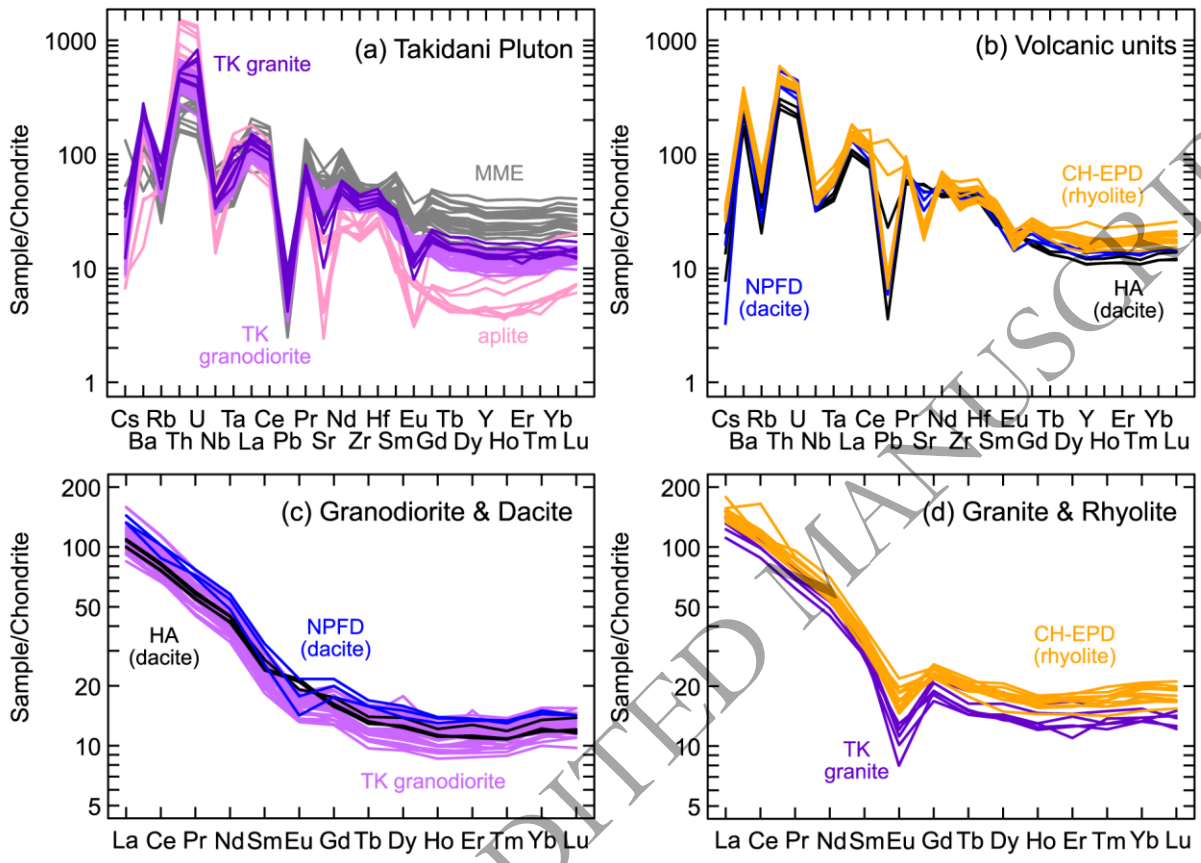

Figure 8.

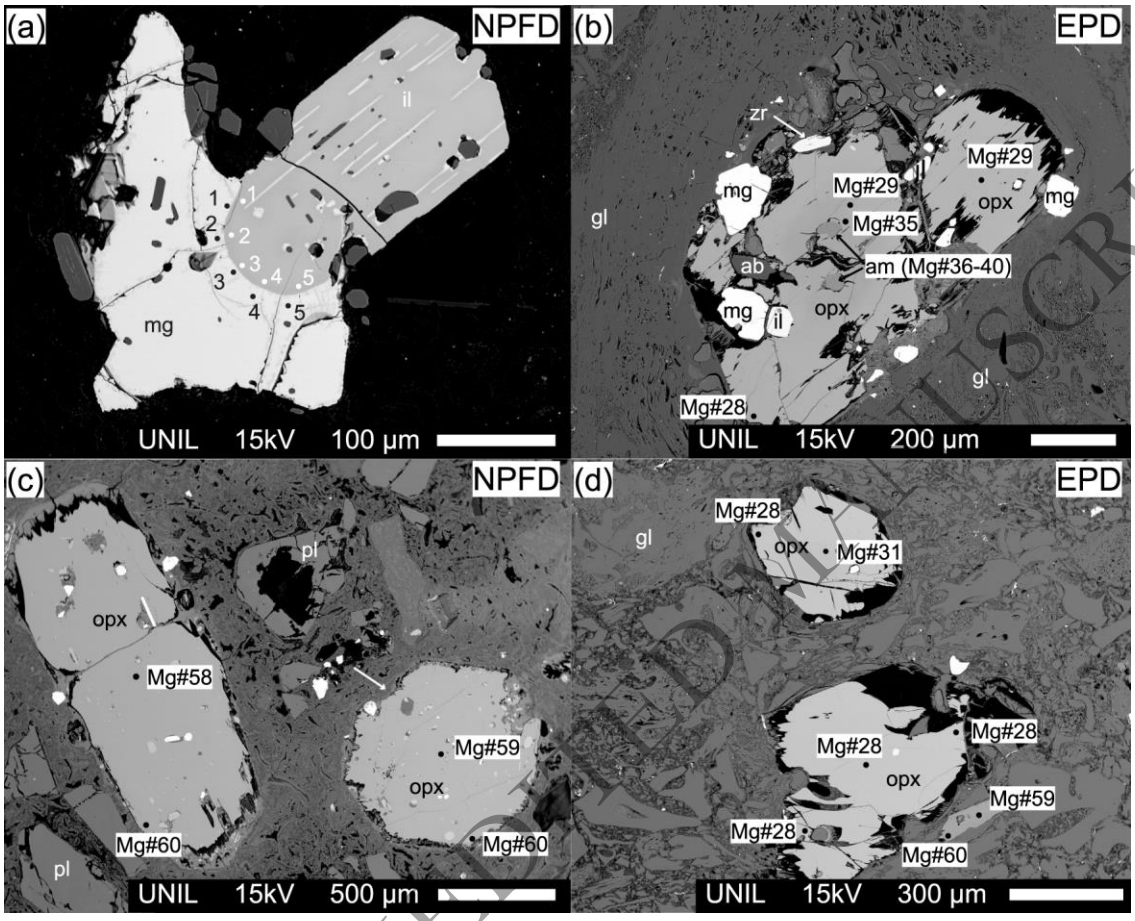

Figure 9.

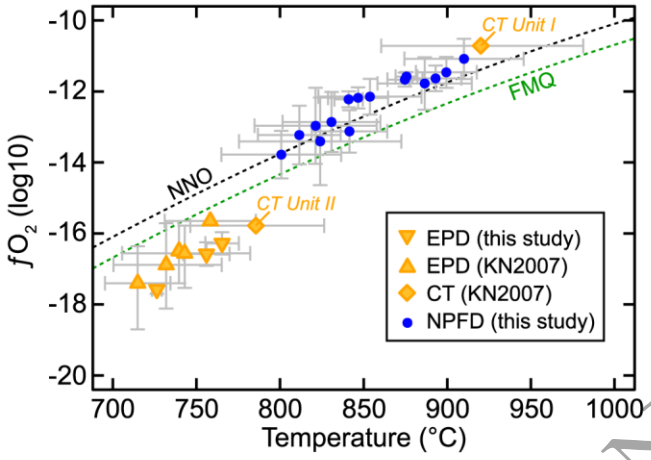

Figure 10.

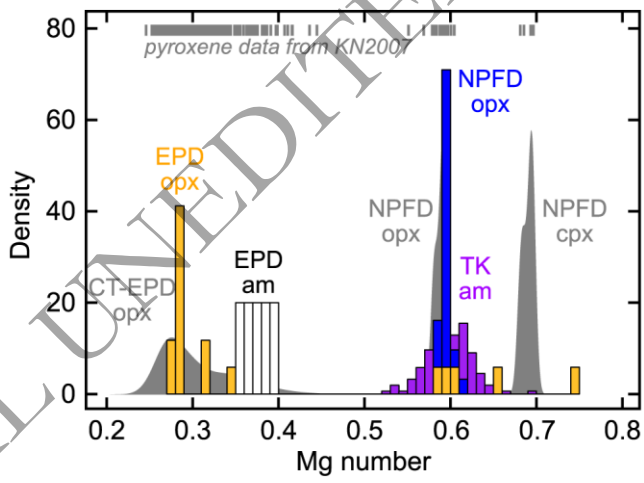

Figure 11.

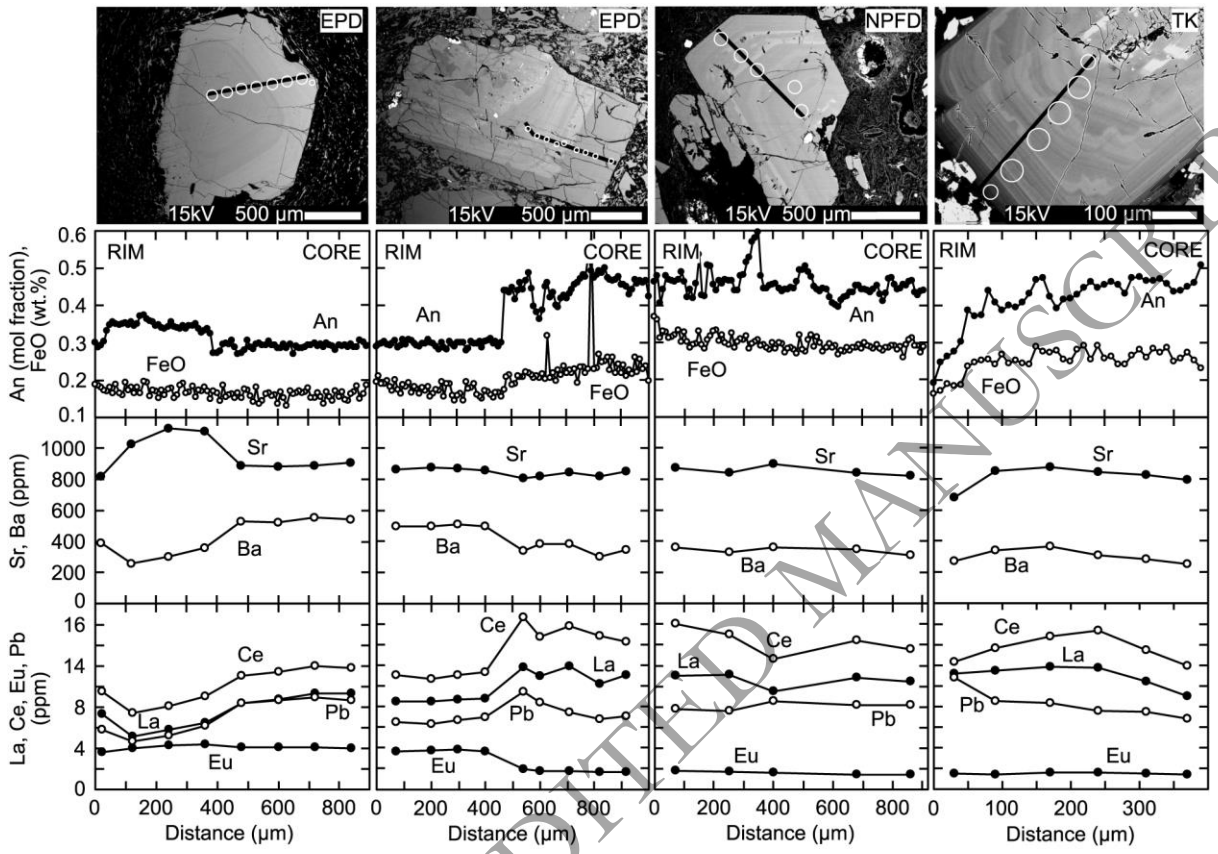

Figure 12.

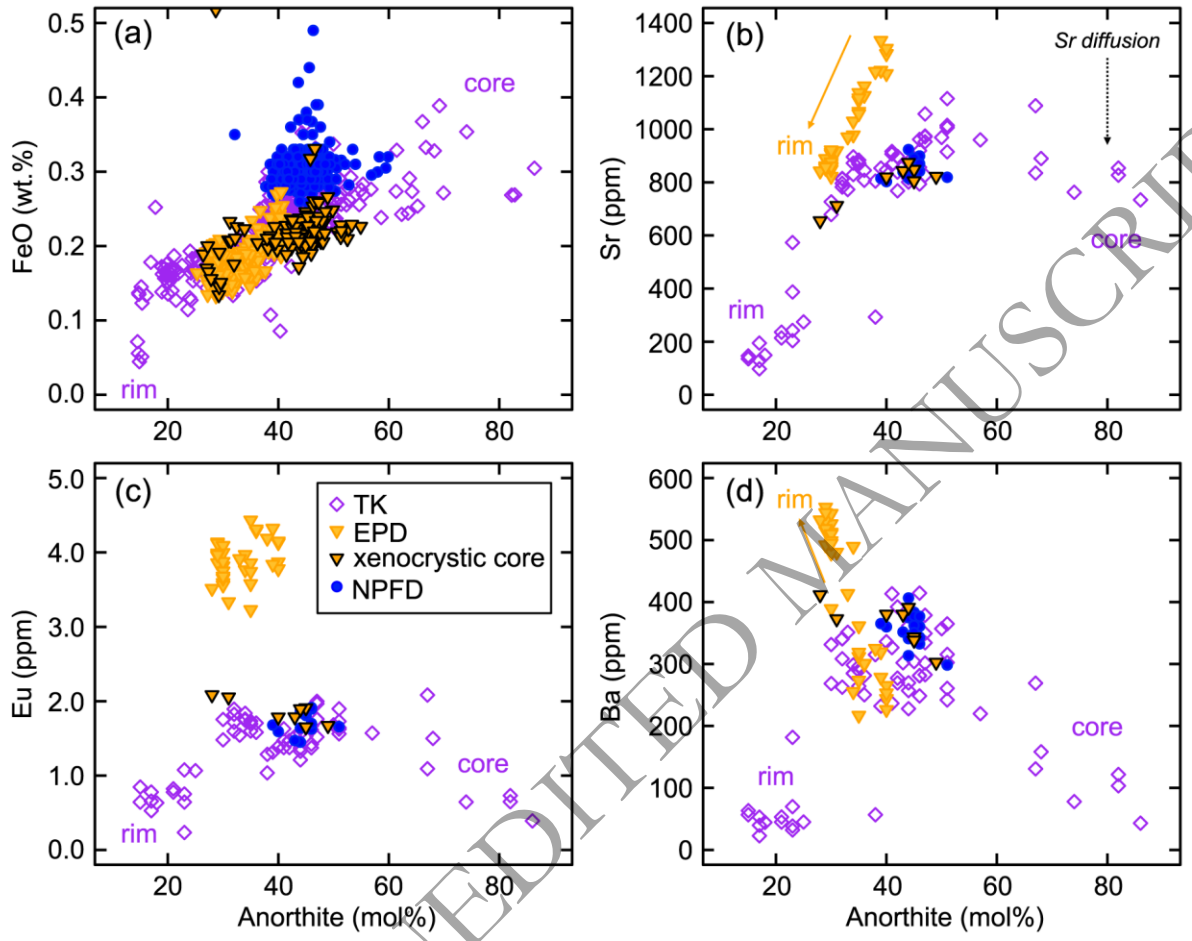

Figure 13.

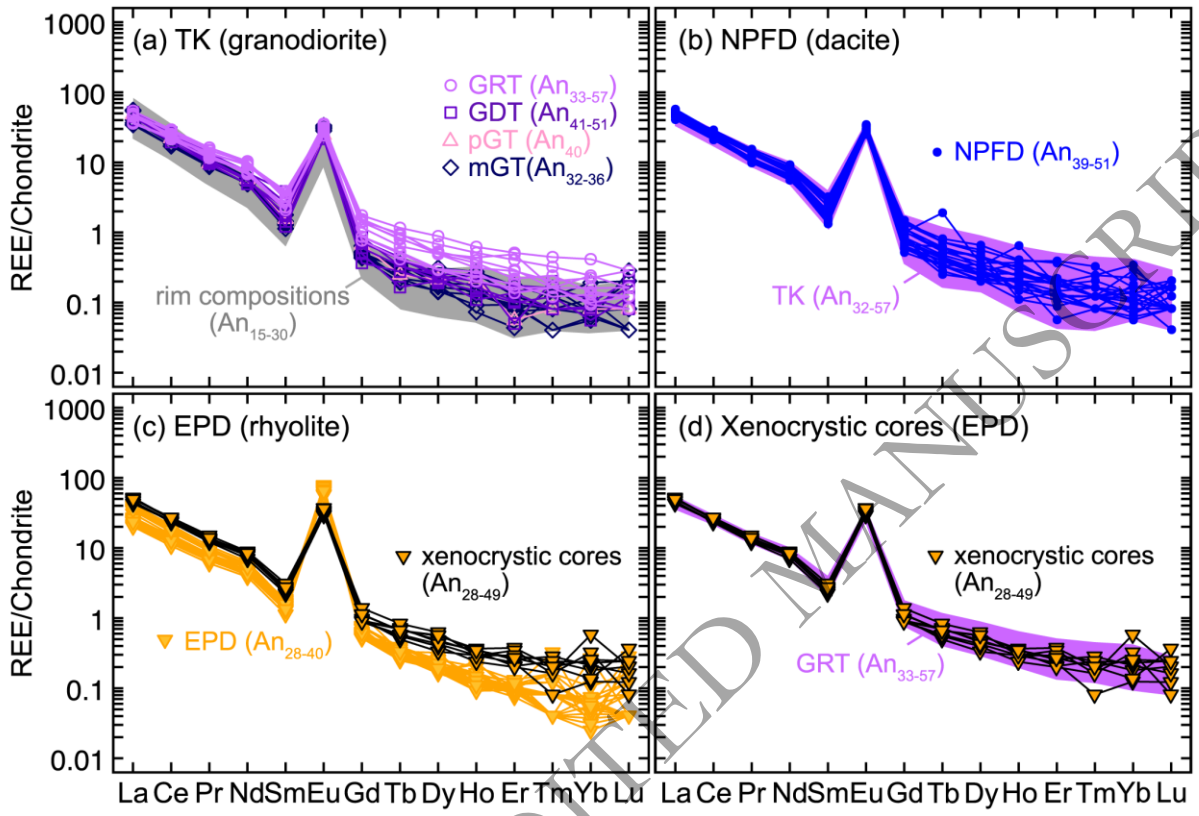

Figure 14.

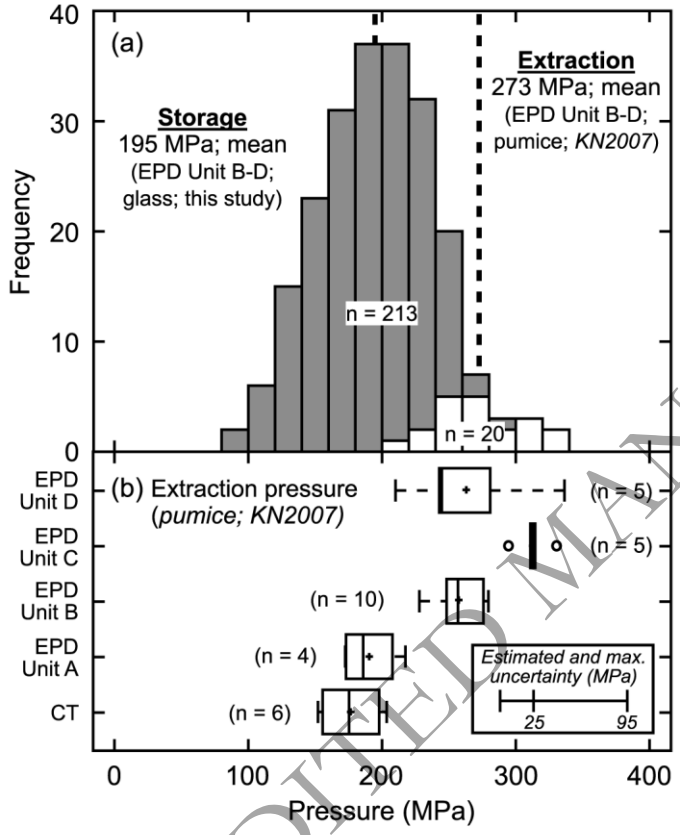

Figure 15.